Hanna Halme

Measuring neural mechanisms of error processing with fMRI: model-based and data-driven methods

School of Electrical Engineering

Thesis submitted for examination for the degree of Master of Science in Technology.

Espoo 10.1.2014

Thesis supervisor:

Prof. Lauri Parkkonen

Thesis advisors:

Docent Iiro Jääskeläinen

Docent Outi Sipilä

Aalto University
School of Electrical
Engineering

AALTO UNIVERSITY
SCHOOL OF ELECTRICAL ENGINEERING

ABSTRACT OF THE
MASTER'S THESIS

Author: Hanna Halme

Title: Measuring neural mechanisms of error processing with fMRI: model-based and data-driven methods

Date: 10.1.2014 Language: English Number of pages:9+58

Department of Biomedical Engineering and Computational Science

Professorship: Biomedical Engineering Code: Tfy-99

Supervisor: Prof. Lauri Parkkonen

Advisors: Docent Iiro Jääskeläinen, Docent Outi Sipilä

Even though processing of errors is one of the most fundamental cognitive functions, it is still unclear whether the human brain processes self-generated and observed errors similarly. In this study, we examined the neural mechanisms of error processing with functional magnetic resonance imaging (fMRI) during self-committed errors, as well as observed errors made by others in both controlled and naturalistic situations. In the first experiment the subjects played a simple response selection game, occasionally making errors. In the second experiment they watched a video recording of the same game played by someone else. In the third experiment they watched short video clips depicting other people failing in everyday situations. The fMRI data were analyzed with the general linear model (GLM) and independent component analysis (ICA) in order to detect error-related activation and functional connectivity. With the third task we also examined the activity caused by error anticipation. In addition, correlations between error-related BOLD responses in 23 predefined regions of interest (ROI) were calculated, and the regional responses in different experimental conditions were compared. Similar activations were detected during self-committed and observed naturalistic errors in striatal subregions (caudate nucleus and globus pallidus), rostral anterior cingulate cortex (ACC) and visual cortical regions. Dorsal ACC, inferior frontal gyrus and insula showed similar activation during self-committed errors and anticipation of naturalistic observed errors. Observed errors in the game could not produce a robust BOLD response. Both ICA and ROI-based analyses indicated high functional connectivity between the key regions of the error monitoring circuit. Together, these findings support the theories advocating distinct functions of rostral and dorsal ACC in error monitoring and suggest that the striatum processes self-generated and observed errors quite similarly.

Keywords: fMRI, event-related, error processing, functional connectivity, anterior cingulate cortex, striatum, naturalistic stimulus, GLM, ICA

AALTO-YLIOPISTO
SÄHKÖTEKNIIKAN KORKEAKOULU

DIPLOMITYÖN
TIIVISTELMÄ

Tekijä: Hanna Halme

Työn nimi: Aivojen virheenkäsittelymekanismien mittaus fMRI:llä: malliin perustuvat ja datalähtöiset menetelmät

Päivämäärä: 10.1.2014 Kieli: Englanti Sivumäärä:9+58

Lääketieteellisen tekniikan ja laskennallisen tieteen laitos

Professuuri: Lääketieteellinen tekniikka Koodi: Tfy-99

Valvoja: Prof. Lauri Parkkonen

Ohjaajat: Dosentti Iiro Jääskeläinen, Dosentti Outi Sipilä

Vaikka virheenkäsittely on eräs tärkeimmistä kognitiivisista toiminnoista, on vielä epäselvää, käsittelevätkö ihmisaivot itse tehtyjä ja havaittuja toisten tekemiä virheitä samalla tavalla. Tässä tutkimuksessa tutkittiin toiminnallisella magneettikuvauksella (fMRI) mekanismeja, jotka liittyvät itse tehtyjen virheiden ja sekä kontrolloiduissa että luonnollisissa tilanteissa havaittujen virheiden käsittelyyn. Ensimmäisessä koeasetelmassa koehenkilöt pelasivat yksinkertaista peliä tehden välillä virheitä. Toisessa kokeessa katseltiin videota kyseisestä pelistä toisen pelaajan pelaamana. Kolmannessa kokeessa katseltiin lyhyitä videopätkiä erilaisista arkielämän virhetilanteista. fMRI-dataa analysoitiin yleisellä lineaarisella mallilla (GLM) ja riippumattomien komponenttien analyysilla (ICA) virhesidonnaisen aivotoiminnan ja toiminnallisen konnektiivisuuden selvittämiseksi. Luonnollisten virheiden ennakoinnin aiheuttamaa aivoaktivaatiota tutkittiin myös erikseen. Lisäksi laskettiin virheiden aiheuttamat hemodynaamiset vasteet 23:lla eri aivoalueella ja tutkittiin eri alueiden vasteiden välisiä korrelaatioita sekä eri koetilanteiden aiheuttamien vasteiden eroja. Itse tehdyt ja luonnolliset havaitut virheet aiheuttivat samanlaista aktivaatiota aivojuovion osa-alueilla (häntätumake ja linssitumakkeen pallo) sekä rostraalisen etummaisen pihtipoimun ja näköaivokuoren alueilla. Dorsaalinen etummainen pihtipoimu, alempi otsalohkon poimu ja aivosaari aktivoituivat samalla tavoin itse tehtyjen virheiden ja luonnollisten virheiden ennakoinnin aikana. Sen sijaan havaitut virheet pelissä eivät aiheuttaneet merkittäviä vasteita. Sekä ICA-tuloksien että yksittäisten aivoalueiden vasteiden korrelaatioiden perusteella virheiden aikana aktivoituneet alueet olivat toiminnallisesti yhteydessä keskenään. Nämä löydökset vahvistavat teorioita rostraalisen ja dorsaalisen etummaisen pihtipoimun erillisistä toiminnoista virheenkäsittelyn aikana ja viittaavat siihen että aivojuovio käsittelee melko samalla tavoin itse tehtyjä ja havaittuja virheitä.

Avainsanat: toiminnallinen magneettikuvaus, tapahtumasidonnainen, virheenkäsittely, toiminnallinen konnektiivisuus, etummainen pihtipoimu, aivojuovio, luonnollinen ärsyke, GLM, ICA

Preface

This work was done in collaboration with the aivoAALTO project at the Department of Biomedical Engineering and Computational Science (BECS) and the Advanced Magnetic Imaging (AMI) Centre of the Aalto University School of Science.

I would like to express my deepest gratitude to my advisor, Docent Iiro Jääskeläinen, for allowing me to work with this interesting research topic, as well as for his patient guidance during this work. I am also grateful to Docent Outi Sipilä for the most valuable and professional advice related to MRI physics. In addition, I would like to thank Professor Lauri Parkkonen for thesis supervision and constructive feedback. I am thankful to all co-workers at the Brain and Mind Laboratory for the relaxed working atmosphere and help in problematic situations. My special thanks go to Karoliina Tapani for assisting me with the fMRI measurements, and Marita Kattelus for helping me to get familiar with the MRI scanner.

Last but not least, I want to thank my family, especially my wonderful parents, who have encouraged me to study natural sciences and inspired me throughout my studies. Finally, thanks to Anton for love, patience and mental support during this demanding thesis work.

Otaniemi, January 10, 2014

Hanna Halme

Contents

Symbols and abbreviations

Symbols

μ	Magnetic moment
B_0	Magnetic field strength
ω_0	Larmor frequency
γ	Gyromagnetic ratio
m_s	Magnetic quantum number
$\hbar$	Reduced Planck's constant
N_{parallel}	Number of particles with spins in parallel orientation
$N_{\text{antiparallel}}$	Number of particles with spins in antiparallel orientation
ΔE	Energy difference between spins in parallel and antiparallel states
$\mathbf{M}$	Net magnetization
B_1	Magnetic field of the RF excitation pulse
θ	Flip angle
T_1	Time constant for longitudinal relaxation
T_2	Time constant for transversal relaxation
T_2*	Time constant for enhanced transversal relaxation
T_2'	Time constant for transversal relaxation caused by field inhomogeneities
x_i	i'th time point
β_i	i'th parameter weight
g_i	i'th covariate
ϵ	Error term
o_j	jth impulse basis function
$\mathbf{x}$	Measured signals
$\widetilde{\mathbf{x}}$	Whitened signals
$\mathbf{A}$	Mixing matrix
$\widetilde{\mathbf{A}}$	Whitened mixing matrix
$\mathbf{W}$	Inverse of the mixing matrix
$\mathbf{s}$	Source signals
$\mathbf{E}$	Eigenvector matrix
$\mathbf{D}$	Diagonal eigenvalue matrix

Operators

$kurt(\cdot)$	Kurtosis
$E\{\cdot\}$	Expected value
$H(\cdot)$	Entropy
$I(\cdot)$	Mutual information
$u(t)$	Stimulus function
$\delta(t)$	Dirac delta function
$h(\tau)$	Hemodynamic function
$f_k(\tau)$	Temporal basis function
$\sum_i$	Sum over index i
$\int_i$	Integral over i

Abbreviations

ACC	Anterior cingulate cortex
BA	Brodmann area
BOLD	Blood oxygen level dependent
CBF	Cerebral blood flow
DAQ	Data acquisition
EEG	Electroencephalography
EPI	Echo-planar imaging
ERN	Error-related negativity
ERP	Event-related potential
FEF	Frontal eye field
FID	Free induction decay
FIR	Finite impulse response
fMRI	Functional magnetic resonance imaging
FOV	Field of view
FWHM	Full width at half maximum
GE	Gradient echo
GLM	General linear model
HRF	Hemodynamic response function
IC	Independent component
ICA	Independent component analysis
IFG	Inferior frontal gyrus
IPL	Inferior parietal lobule
ISI	Interstimulus interval
LPFC	Lateral prefrontal cortex
MDL	Minimum description length
MEG	Magnetoencephalography
MNI	Montreal Neurological Institute
MPFC	Medial prefrontal cortex
MPRAGE	Magnetization prepared rapid acquisition gradient echo
MR	Magnetic resonance
MRI	Magnetic resonance imaging
Ne	Error negativity
NMR	Nuclear magnetic resonance
OCD	Obsessive–compulsive disorder
PCA	Principal component analysis
PCC	Posterior cingulate cortex
PD	Parkinson's disease
PET	Positron emission tomography
RF	Radio frequency
ROI	Region of interest
SE	Spin echo
SEM	Standard error of the mean
SMA	Supplementary motor area
SNR	Signal-to-noise ratio
SPM	Statistical parametric mapping
STG	Superior temporal gyrus
TE	Echo time
TI	Inversion time
TR	Repetition time

1 Introduction

Error processing is one of the most fundamental cognitive functions. Evaluation of action outcomes and dynamic adjustment of behavior are required for adaptation to the constantly changing environment. As humans learn by the consequences of their actions, error monitoring is the core function for reinforcement learning. Impaired error processing has been related to several psychiatric disorders characterized by maladaptive behavior, including Parkinson's disease [Falkenstein et al., 2001; Ito and Kitagawa, 2006; Willemssen et al., 2008], schizophrenia [Manoach and Agam, 2013; Sanders et al., 2002], obsessive–compulsive disorder [Fitzgerald et al., 2005] and depression [Gotlib et al., 2005].

Anterior cingulate cortex (ACC) has been found to mediate error processing and modulate the activity of prefrontal executive regions, thus controlling the behavioral adjustments after mistakes (see the reviews by van Veen and Carter [2002] and Bush et al. [2000]). However, it is still unclear whether the function of ACC and other regions of the error-monitoring brain circuit is similar during self-committed and observed errors. Growing body of evidence suggests that the human brain processes action execution and action observation in a similar way. Therefore, it is likely that observed errors will activate the same brain regions as the self-committed errors.

In conventional neuroscientific research, brain functions have been studied with relatively simple stimuli, and the responses have mostly been modelled with the general linear model (GLM). However, during recent years the focus in neuroscience has increasingly shifted towards naturalistic stimulus paradigms. Instead of using highly controlled stimuli, many research groups have adopted rather complicated, multisensory tasks, such as video games and movies. Naturalistic stimuli are able to activate widely distributed neural networks related to higher-order cognitive functions [Spiers and Maguire, 2007]. Furthermore, the activation of a certain brain network in response to naturalistic stimuli verifies that the same network is most likely activated also in real life under similar conditions. Therefore, brain mechanisms observed in laboratory conditions can be generalized into natural, everyday environments. This higher ecological validity is a great advantage when investigating behavioral deficits that only arise during complex cognitive tasks, such as social interaction.

It is still somewhat uncertain whether naturalistic stimuli, such as movie clips, are capable of eliciting robust error-related brain activity. To date, it has not been directly tested whether the activation patterns caused by observed errors are similar during controlled and naturalistic experiments. It can be hypothesized that watching a failure in a naturalistic scene, for example someone falling down, causes increased emotional responses compared to seeing an error in a simulated video game. Thus, we can expect enhanced error-related activation during the naturalistic scenario, especially in the regions related to emotional processing.

Because of the high complexity of naturalistic paradigms, novel signal analysis methods have been developed to uncover the neural responses related to rich multisensory stimuli [Malinen et al., 2007]. Individual and regional variability of the BOLD response would decrease detection efficiency if a standard hemodynamic re-

sponse function was used as a regressor. Modifications of the standard HRF, for example the finite impulse response (FIR) basis functions, are able to account for this variability. With a FIR regressor model it is possible to capture event-related responses with any shape up to a predefined time scale. Another approach for analyzing complex activation patterns is to use data-driven methods, which do not make any *a priori* hypotheses about the measured signals, but rather attempt to detect underlying signal structures. Independent component analysis (ICA) is the most popular method for spatio–temporal segregation of activation patterns from fMRI data. The main advantage of ICA is the ability to extract confounding signal sources, such as physiological noise, head movements and scanner noise, which would bias the GLM estimates if not specifically modelled in the design matrix. Furthermore, ICA can detect brain activity unrelated to the task, whereas GLM only models the predefined task effects. Because the regions belonging to the same component share the same activation pattern, they are assumed to be functionally interconnected. ICA is thus also a straightforward measure of functional connectivity.

The main goal of this study is to examine whether committing and observing errors elicit similar neural activity. We measure blood oxygen level dependent (BOLD) responses while the subjects make errors themselves and observe mistakes by others in both controlled and naturalistic conditions. In addition, we aim to establish the effect of error anticipation on error-related BOLD responses. By contrasting the BOLD responses caused by anticipation and observation of errors in the naturalistic condition, we can examine whether the error response is elicited specifically by the likelihood of an error or the occurrence of a failure. In addition, responses to expected and unexpected errors can be extracted and contrasted with each other, which enables studying the effect of surprise to the error responses. Another objective of this study is to compare the results of GLM and ICA analyses applied to an event-related fMRI paradigm. With the combined results from these two methods, we aim at examining whether the brain regions showing significant error-related activation are also functionally connected during error monitoring.

2 Neural basis of error processing

Detecting and correcting errors is an important function for adaptive goal-directed behavior. This section introduces the anatomical regions involved in error monitoring and discusses recent theories about the cognitive processes underlying error detection. Furthermore, the chapter briefly discusses processing of observed errors. Finally, we review recent findings on error-processing deficits related to several neuropsychiatric disorders, since there are important correlations between brain structural abnormalities and error monitoring deficits.

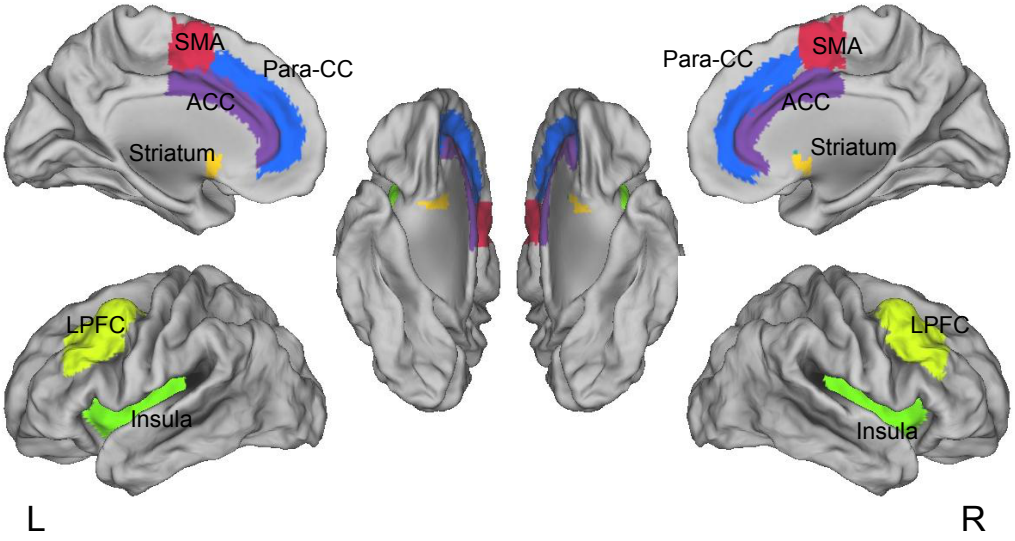

Figure 1: Brain regions contributing to error processing. ACC = anterior cingulate cortex, Para-CC = paracingulate cortex, SMA = supplementary motor area, LPFC = lateral prefrontal cortex.

2.1 Neuroanatomical circuits involved in error monitoring

Efficient error monitoring requires the cooperation of widespread frontal and frontostriatal brain circuits [Ullsperger and von Cramon, 2006]. Figure 1 represents some key regions which have been found to contribute to error processing. Electrophysiological, neuroimaging and lesion studies have established the central role of the anterior cingulate cortex (ACC) in supporting error processing. A vertex-transvert response peaking at 100–150 ms after error commission has frequently been detected in event-related potential (ERP) studies using electroencephalography (EEG) and magnetoencephalography (MEG). This error-related negativity (ERN/Ne), described first by Gehring et al. [1993] and Hohnsbein et al. [1989], has been localized in ACC or medial frontal cortex using dipole modeling. Neuroimaging findings have confirmed the contribution of ACC to error monitoring. Several fMRI studies have found increased activity in ACC during error commission compared to successful

performance [Braver et al., 2001; Carter, 1998; Kiehl et al., 2000; Menon et al., 2001; Ullsperger and von Cramon, 2001]. Importantly, the increased activity has been observed in a wide variety of error tasks, indicating an underlying general error detection mechanism modulating responses according to the goals of the current task.

ACC is located on the medial surface of the frontal lobe and surrounds the frontal part of the corpus callosum. It can be anatomically divided into dorsal and rostral regions. The dorsal part of ACC (dACC) extends caudally from the genu of the corpus callosum into the anterior commissure, and shares connections with the striatum, lateral prefrontal cortex (LPFC), frontal eye fields (FEF) and supplementary motor area (SMA) [Paus, 2001]. The extensive connectivity with these executive brain regions makes dACC a central modulator for planning, generation and execution of actions. Error-related activation of dACC is observed in several fMRI studies [Taylor et al., 2006; van Veen and Carter, 2002], proposing that the behavioral adjustments after error commission are controlled by that region.

The rostral part of the ACC is (rACC) lies anterior and ventral to the genu of the corpus callosum. It is connected to the orbitofrontal cortex, as well as several limbic and paralimbic regions, including amygdala, hypothalamus, insula and nucleus accumbens. In addition, rACC receives input from several thalamic nuclei, as well as pre-supplementary motor area (pre-SMA) and dorsal premotor cortex. In addition, rACC and pre-SMA are connected with the lateral prefrontal cortex (LPFC). LPFC projects further to the basal ganglia, especially to the rostral striatum [Ullsperger and von Cramon, 2006]. The diverse neural inputs from limbic regions involved in directing motor behavior allow rACC to combine emotional and nociceptive information about action outcomes. This information is further used by the prefrontal cortex to coordinate behavior. Several fMRI studies [Garavan et al., 2002; Menon et al., 2001; Polli et al., 2005] have found increased error-related activation of rACC and interconnected regions, especially insula and amygdala. Increased activation of rACC and affective regions due to error commission is assumed to reflect the emotional significance of errors [Bush et al., 2000; Manoach and Agam, 2013]. In particular, considering the large reciprocal connections between rACC and insula and the conjoint activity of these regions observed after error commission (see a review by Medford and Critchley [2010]), it it assumed that they constitute a core network involved in awareness and subjective feelings of errors.

The segregation between dorsal 'cognitive' and rostral 'emotional' parts of the anterior cingulate cortex has been the predominant theory so far. However, in recent years a growing body of evidence has suggested an integration of negative emotional responses, cognitive control and monitoring of pain in the dACC (see a review by Shackman et al. [2011]). Thus, the cognitive and emotional functions subserved by the ACC are not strictly localized to its subregions, but instead might be integrated over extensive cortical and subcortical networks.

2.2 Cognitive processes underlying error monitoring

There is an ongoing debate about the exact neural processes involved in error monitoring (see a review by Ullsperger and Von Cramon [2004]). Holroyd and Coles [2002] proposed that the error signals causing the ERN are controlling reinforcement learning. According to this theory, the midbrain dopamine system induces a negative reinforcement signal after error commission into the frontal cortex, which disinhibits the dendrites of neurons in the motor cortex extending into the ACC. The disinhibition elicits the ERN and increased post-error BOLD activity in the ACC. The dopaminergic neurons respond to differences in the predictions of events, increasing or decreasing activity for events that are better or worse than expected, respectively. The theory was refined by Alexander and Brown [2011], who proposed a unified model for ACC/mPFC activation in evaluating predicted response outcome. Importantly, the midbrain dopamine system may activate due to anticipation of reward or punishment, in addition to already committed errors or successive trials. This anticipation signal is used to modulate other brain regions involved in reinforcement learning [Holroyd and Coles, 2002].

Another theory states that error signals are related to conflicting responses. A classical example of a response conflict is the Stroop task, in which the subject has to name the ink color, instead of reading the text depicting the name of the color. As the subject has to withhold the congruent response (reading the text) and execute the incongruent response (detect the ink color), both responses are activated at the neural level. ACC activity increases due to the incompatible responses and interacts with prefrontal control regions in order to strengthen the focus on the current task. The response conflict theory was established in an ERP study by van Veen and Carter [2002], who observed a vertex-negative peak both after errors and 340–380 ms after trial onset, the latter being increased for conflict trials. Importantly, both peaks had a source in ACC. Further studies [Botvinick et al., 2001; Egner et al., 2007; van Veen and Carter, 2005] have refined the conflict-processing hypothesis and confirmed that both response conflict and incongruent stimuli activate separate, nonoverlapping ACC and dorsolateral prefrontal cortex (dLPFC) regions.

The third theory about error processing considers the motivational and affective significance of errors. Gehring et al. [1993] found that the ERN amplitude is higher when the participants were more engaged to the task, i.e. when motivational significance was higher. This finding suggests that the error detection mechanism is also dependent on the salience of the error stimulus. This effect is largely explained by the anatomical connections between rACC and the limbic regions.

2.3 Processing of observed errors

Neural correlates of observed errors have been investigated in several studies. Observing errors made by someone else produces a similar ERN as self-generated errors [Miltner et al., 2004; van Schie et al., 2004; Yu and Zhou, 2006]. Recent fMRI studies [de Bruijn et al., 2009; Schiffer et al., 2013; Shane et al., 2008] have localized the activation to medial prefrontal cortex (MPFC) or rostral cingulate, a region also

responding to self-generated errors. These findings suggest a similar neural mechanism for processing both self-committed and observed errors. Importantly, it seems that the rACC/MPFC has specialized to detection of incorrect events, regardless of the reward value associated with them; in the fMRI study by de Bruijn et al. [2009] the region showed increased activation after errors made by both cooperators and enemies.

There is evidence that observed errors also affect the activity in the midbrain dopamine system subserving reward and punishment. Kätsyri et al. [2013] showed that striatal responses were more pronounced during active playing of a video game than passive watching of the recorded game, both during wins and losses. Importantly, in their study both wins and losses produced striatal deactivation, which was more significant after successful events. A controversial finding was documented by de Bruijn et al. [2009], who found increased striatal activity after correct self-made responses and errors made by the enemy.

Furthermore, the effect of error anticipation has been studied in order to specify whether the error response arises specifically due to surprising events or incorrectness of actions. Self-committed errors are always surprising, but errors made by others can sometimes be predicted, which enables studying the distinction between these two aspects of error processing. Also, if the unexpectedness of errors was the main contributor to the ERN or related BOLD responses, similar brain activation would be elicited by unexpected correct events. Schiffer et al. [2013] investigated this possibility in an fMRI study and found that the rostral cingulate zone (located close to the dACC/SMA despite its name) activates specifically after unexpected events, regardless of their correctness.

2.4 Error monitoring deficits in neuropsychiatric disorders

The dysfunction of error-processing circuits has been associated with a number of neuropsychiatric disorders. Studying patients with known deficits in parts of the error monitoring system can shed light on the neural correlates of error processing. Furthermore, comparing the activation patterns of patients to those of healthy subjects can help in identifying the differences contributing to the behavioral abnormalities in neuropsychiatric disorders. Correctly detecting the dysfunctional neural mechanisms is important when designing treatment and rehabilitation, and studying these mechanisms thoroughly on healthy subjects constitutes the basis for clinical research. This section briefly reviews recent findings about certain error processing pathologies.

Error detection abnormalities have been detected in patients with Parkinson's disease (PD), a neurodegenerative disorder causing the loss of dopaminergic neurons in the basal ganglia. Because PD causes deficits in dopamine release especially in the dorsal striatum, error processing abnormalities can be directly related to dysfunction of that region. ERN amplitude is reduced in non-demented PD patients compared to healthy controls [Falkenstein et al., 2001; Ito and Kitagawa, 2006; Willemssen et al., 2008]. Blunted ERN has also been observed in patients with Huntington's disease [Beste et al., 2006], a neurodegenerative disorder particularly affecting the striatum.

Together, these findings support the theory about the essential contribution of basal ganglia and midbrain dopaminergic neurons in error monitoring.

The inability to detect inconsistencies between goals and behavior has been suggested to underlie both positive and negative symptoms in schizophrenia (see a review by Sanders et al. [2002]). Positive symptoms include delusions and hallucinations, which may reflect a misattribution of internal thoughts to external sources [Mathalon et al., 2002]. Negative symptoms, such as poverty of speech, anhedonia, lack of motivation and social exclusion, are likely related to dysfunction of the rostral affective division of ACC and impaired regulation of the limbic system. Previous neuroimaging and ERP studies have shown evidence of ACC dysfunction in schizophrenia. Carter et al. [1997] found ACC underactivation during response conflict in a PET study of schizophrenic patients. Reduced ERN amplitude related to schizophrenia has been observed by Laurens [2003], Kopp and Rist [1999] an by Mathalon et al. [2002]. Furthermore, Polli et al. [2008] found decreased error-related BOLD activity in both dorsal and rostral ACC.

In contrast to the decreased error-related brain activity in schizophrenia, hyperactivation of ACC has been observed in patients with obsessive–compulsive disorder (OCD) during error detection [Fitzgerald et al., 2005]. ACC hyperactivity increases with symptom provocation and decreases during successful treatment. Oversensitivity to errors is a likely cause for obsessive thoughts and compulsive behavior aiming to correct the perceived mistakes. Both response conflict and error commission have been found to cause increased ACC activation in OCD patients [Ursu et al., 2003]. In addition, patients with major depression show increased activity of subgenual ACC in response to emotional stimuli [Gotlib et al., 2005]. In conclusion, increased error-related activation of ACC, especially the subgenual part, causes enhanced emotional responses to errors, which likely contributes to the development of OCD and mood disorders.

3 Functional magnetic resonance imaging

This section introduces the basic terms and concepts related to functional magnetic resonance imaging (fMRI), largely based on the textbook of Huettel et al. [2004]. The principles of nuclear magnetic resonance, MR image formation, hemodynamic response, BOLD signal generation, noise sources in fMRI and preprocessing of fMRI data are briefly reviewed.

3.1 Nuclear magnetic resonance

Nuclear magnetic resonance (NMR) of atomic nuclei constitutes the basis for magnetic resonance imaging. Many particles have an intrinsic magnetic property called spin, causing their magnetic interaction with each other and external magnetic fields. Atoms with a nonzero spin (i.e. an odd number of protons or neutrons) have a magnetic moment μ. An atom has to have both an angular momentum and a magnetic moment in order to possess the NMR property, which enables their use in MRI.

The hydrogen nucleus, consisting of a single proton, is the most frequent nucleus in human body and therefore the most commonly utilized in human MRI. The spins of protons are normally randomly oriented. In an external magnetic field B_0, the spins experience a torque, which causes them to align in the direction of B_0 and start precessing around their axis at a nucleus-specific frequency ω_0, called *Larmor frequency*

$$\omega_0 = 2\pi f = \gamma B_0 \tag{1}$$

where γ is the gyromagnetic ratio. The z-component of the magnetic moment μ in an external magnetic field can have values

$$\mu_z = \gamma m_s \hbar \; m_s = -s, -s+1, ..., s, ... \tag{2}$$

where $\hbar = h/2\pi$, h is Planck's constant, and m_s is the magnetic quantum number.

Because for hydrogen $m_s = 1/2$, the magnetic moment vector has two possible orientations: either parallel or anti-parallel with B_0, antiparallel being the state with a higher energy. There are always more nuclei in the parallel state, and the relative proportion of spins in these two states depends on their energy difference ΔE and the absolute temperature T

$$N_{\text{parallel}}/N_{\text{antiparallel}} = e^{\Delta E/kT} \tag{3}$$

where k is Boltzmann's constant.

The net magnetization $\mathbf{M}$ is a vector describing the overall magnetization of a spin system, i.e. the sum of magnetic moments of all spins within an imaging volume. The magnitude of $\mathbf{M}$ is proportional to the difference between the number of spins in parallel (N_{parallel}) and antiparallel ($N_{\text{antiparallel}}$) states, and it is linearly dependent on the strength of the external field:

$$\mathbf{M} = (N_{\text{parallel}} - N_{\text{antiparallel}})\mu_z \mathbf{z} \tag{4}$$

where $\mathbf{z}$ is a unit vector in the z-direction, i.e. the direction of B_0.

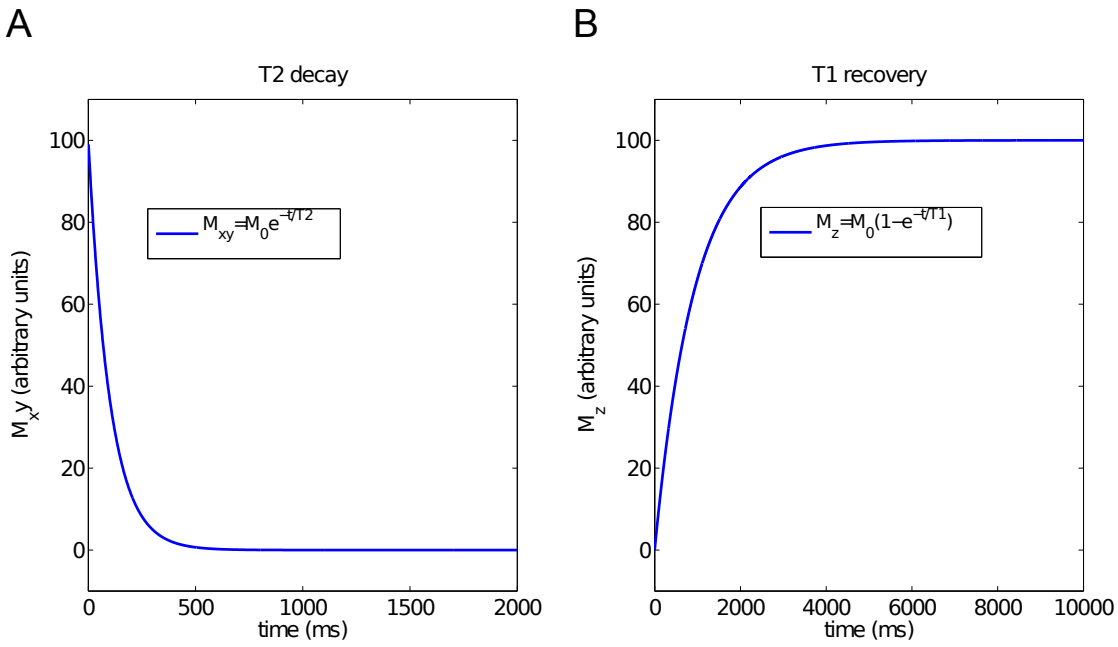

Figure 2: A) T_2 decay describes the loss of transverse magnetization M_{xy} as a function of time. B) T_1 describes the recovery of the longitudinal magnetization M_z.

3.2 Excitation and relaxation

During MRI, a net magnetization vector is tipped away from the direction of B_0 by applying a radiofrequency (RF) electromagnetic pulse orthogonally to B_0. Flip angle θ is the resulting angle between the net magnetization vector and B_0, and its magnitude is proportional to the amplitude and duration of the RF pulse. The magnetic field of the RF pulse is commonly referred to as B_1.

The precession of the net magnetization vector creates a time-varying magnetic field, which induces a current in the receiver coil. As soon as the excitation pulse is turned off, the net magnetization starts to lose phase coherence and return to equilibrium. As a result of this process, referred to as relaxation, the measured current begins to decay and produces a free induction decay (FID) signal. Usually this immediate signal decay is not recorded but instead, an echo of the original signal is produced by refocusing the spins shortly after excitation. In a spin echo (SE) pulse sequence, a 180° RF pulse is used for refocusing the spins, setting them maximally in phase after the echo time (TE). In a gradient echo (GE) sequence, a gradient field is used for dephasing the spins and an opposite gradient field for refocusing them after a short time period; the refocusing gradient generates the echo.

The excited nuclei return to equilibrium by two distinct decay mechanisms, characterized by the two relaxation time constants. Because of the decay, the RF pulses must be applied repetitively to elicit new MR signals. The time between two consecutive excitation pulses is called the repetition time (TR). The gradual loss of phase

coherence due to spin–spin interactions is described by the time constant T_2 and the recovery of longitudinal magnetization by the time constant T_1 (see Fig. 2).

The processes of precession and relaxation are described by Bloch equations:

$$\frac{dM_x}{dt} = \gamma B_0 M_y - \frac{M_x}{T_2} \tag{5}$$

$$\frac{dM_y}{dt} = -\gamma B_0 M_x - \frac{M_y}{T_2} \tag{6}$$

$$\frac{dM_z}{dt} = -\frac{M_z - M_0}{T_1} \tag{7}$$

Inhomogeneities in the magnetic field over time cause minor differences in precession frequency of different nuclei. The total relaxation resulting from spin–spin relaxation time T_2 and field inhomogeneities T_2' is described by T_2^*.

$$\frac{1}{T_2^*} = \frac{1}{T_2} + \frac{1}{T_2'} \tag{8}$$

T_2^* contrast can only be obtained with gradient echo (GE) imaging, because the 180° pulse in the spin echo sequence eliminates the transverse relaxation caused by field inhomogeneities (see a discussion by Chavhan et al. [2009]). T_2^* relaxation is important for fMRI, since it causes a very rapid loss of spin coherence and enables quick signal acquisition.

3.3 Signal generation

The MR signal strength is proportional to the strength of B_0 and the tissue-specific relaxation times. The magnitude of signal strength can be derived from the Bloch equation:

$$\frac{d\mathbf{M}}{dt} = \gamma \mathbf{M} \times \mathbf{B} + \frac{1}{T_1}(\mathbf{M}_0 - \mathbf{M}_z) - \frac{1}{T_2}(\mathbf{M}_x + \mathbf{M}_y) \tag{9}$$

where $\mathbf{B}$ contains the sum of all magnetic fields, including the static field $\mathbf{B_0}$, the RF excitation pulse $\mathbf{B_1}$, gradient fields and field inhomogeneities.

Because the relaxation times contribute to the signal strength, they can be utilized to make contrast between different tissue types in the MR images. Contrast is maximized by collecting the signal when there is the largest difference in magnetization between different tissue types. If the difference is mainly caused by the longitudinal magnetization decay (the effect of T_1 relaxation), the contrast is T_1 weighted. T_2 weighted contrast is obtained when the difference is mainly caused by the transverse decay.

In the case of fMRI, T_2^* relaxation is the most important contrast mechanism. The maximum contrast is achieved with a long TR (2–3 s) and a short TE (around 30 ms), such that the differences in T_2^* effects between oxygenated and deoxygenated blood are maximized.

3.4 Image formation

Besides flipping the net magnetization with RF pulses, the contribution of each voxel to the total MR signal has to be uniformly encoded before the image can be constructed. The encoding is done by introducing gradient magnetic fields, which are turned on and off in z-, x- and y-directions in a controlled sequence to measure the signal in each individual voxel. This encoding procedure is referred to as a pulse sequence.

As the precession frequency is proportional to the strength of the external magnetic field, spatially varying gradient fields cause the precession frequency to vary linearly as a function of the location. Therefore, an excitation pulse given at a certain frequency band will only excite protons corresponding to that frequency within a certain 2D slice. This process is called slice selection, and it determines the location of spins in z-direction, i.e. along the axis of B_0.

Immediately after slice selection, the location in x- and y-directions is selected by introducing additional frequency- and phase-encoding gradients. Phase encoding means applying a gradient $G_y(t)$ in the y-direction slightly before frequency encoding, such that the spins differ in phase of precession when the other gradient is applied. Applying a frequency-encoding gradient $G_x(t)$ in the x-direction produces varying precession frequencies for spins along that direction. It should be noted that in practice the slice selection, frequency encoding and phase encoding gradients can be applied to any arbitrary direction; the directions described here were just examples to simplify the theory. As a result, spins at each location of the two-dimensional slice have a unique combination of precession frequency and phase. The information about frequencies and phases is collected in k-space [Ljunggren, 1983], and the final image is reconstructed by the Fourier transform.

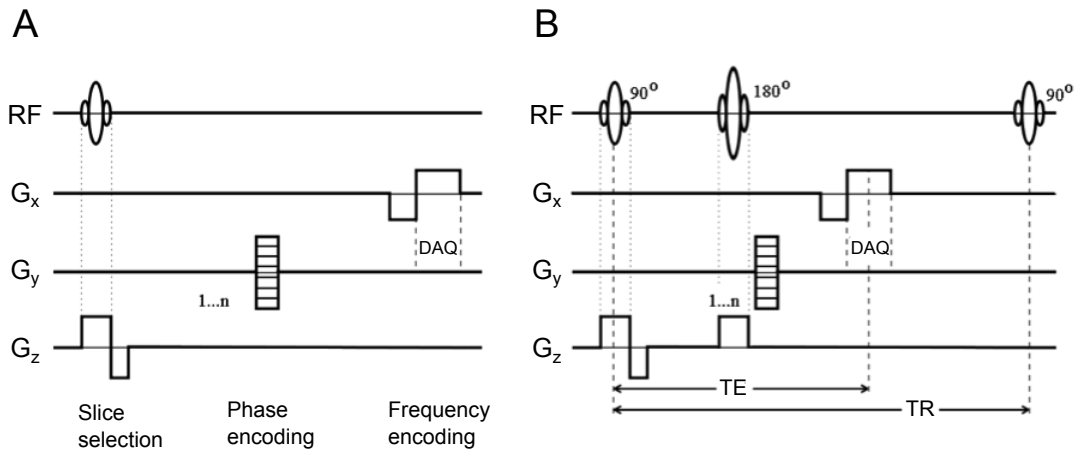

Figure 3: A) A gradient-echo sequence illustrating the gradients G_x, G_y and G_z during the imaging process and the data aqcuisition (DAQ) period. B) A spin-echo sequence illustrating the imaging parameters TE and TR. Figure modified from [Lahnakoski, 2010].

The resolution along the phase-encoding direction determines the number of excitations needed for collecting an image: the size of the imaging matrix is equal to the number of separate excitations with a different phase-encoding gradient. In fast imaging techniques, such as most sequences used in fMRI, frequency and phase gradients are applied simultaneously, and the gradients oscillate rapidly over the acquisition period.

3.5 BOLD and hemodynamic response

Activation of neurons in response to external and internal stimuli increases their metabolism, which results in an increased flow of oxygenated blood to the active brain regions. This phenomenon is called the hemodynamic response. The increased neural activity causes cerebral blood flow to rise more rapidly than the metabolic consumption of oxygen in the neurons, resulting in an increased local concentration of oxygenated hemoglobin. Because hemoglobin is diamagnetic when oxygenated and paramagnetic when deoxygenated, this overshoot of oxygenated hemoglobin alters the local magnetic susceptibility, reduces local magnetic field distortions and causes a minor increase in the local MR signal. This slight increase constitutes the basis for the electromagnetic signal measured during fMRI, referred to as blood oxygen level dependent (BOLD) signal [Ogawa et al., 1990]. The effect of neural responses to the increase of BOLD signal was first documented by Kwong et al. [1992].

BOLD is an indirect measure of the underlying neural activity, and its magnitude is affected by a number of physiological factors, including changes in cerebral blood flow, cerebral blood volume and oxygen metabolic rate. Since the changes can vary to a great extent between brain regions and individuals, it is not convenient to measure the exact physiological responses caused by certain stimulus patterns. Instead, mathematical models for the hemodynamic response function (HRF) are used for detecting changes in brain activity. By modeling the HRF with appropriate functions it is possible to detect regions in which the activation patterns are significantly correlated with the stimulus paradigm.

3.6 Echo-planar imaging

Echo-planar imaging (EPI), originally introduced by Mansfield [1977], is currently the most popular imaging sequence in fMRI. EPI allows rapid image acquisition and sufficient spatial resolution for functional images. Whole-brain images can be acquired within a single TR of 2–3 s. This temporal resolution is sufficient for detecting changes in brain hemodynamics, which typically occur within a few seconds from the stimulus onset.

EPI is performed by collecting multiple lines of imaging data after a single excitation RF pulse [Poustchi-Amin et al., 2001]. A train of gradient echoes is formed by rapidly oscillating gradients, and all phase-encoding steps are acquired within one TR. Because the RF refocusing pulse is not applied, gradient echo EPI is sensitive to T_2^* decay [Chavhan et al., 2009]. The rapid switching of gradients requires a

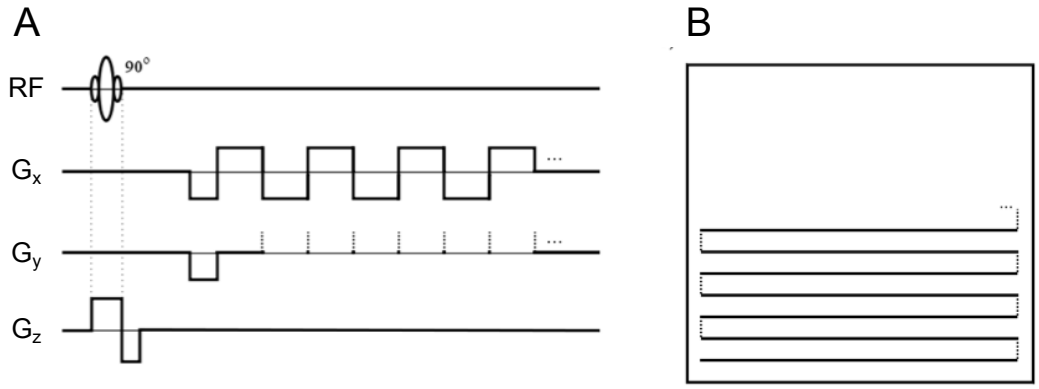

Figure 4: A) An illustration of an EPI pulse sequence. B) The corresponding k-space trajectory. Figure modified from [Lahnakoski, 2010].

strong gradient system of at least 25 mT/m [Huettel et al., 2004], which is nowadays implemented in most MRI scanners used for clinical and research purposes.

EPI enables a very fast image collection, but both resolution and SNR are poor compared to standard SE and GE sequences. EPI images typically have a spatial resolution of 3-4 mm. Therefore, statistical maps of functional images are usually overlaid on anatomical high-resolution images in order to localize brain activations.

Higher resolution and better image quality (decreased distortion and signal loss due to susceptibility differences, T_2 relaxation and main field inhomogenity) can be achieved by using multiple RF pulses instead of a single one. However, the single-shot technique is more commonly used. EPI is sensitive to off-resonance artifacts due to the lack of refocusing pulses. A usual artifact in EPI images is a chemical shift due to fat protons, and therefore fat suppression techniques are used by default in most EPI types [Huettel et al., 2004].

3.7 Noise sources in fMRI

Signal-to-noise ratio (SNR) in general defines the proportion of signal intensity inside the imaged object and the signal outside the object. However, in fMRI the SNR usually describes the intensity of the signal originating from the neural process of interest divided by the intensity of other signal sources, such as the brain activity unrelated to the stimuli. Noise in fMRI can arise from thermal fluctuations within the subject and scanner electronics, discrepancies in scanner hardware, artifacts originating from physiological processes and subject motion, and variations in the intrinsic neural activation [Huettel et al., 2004].

Thermal noise occurs as the electrons collide with atoms within the scanner and subject, and it increases linearly with temperature and field strength [Huettel et al., 2004]. Thermal noise is uniformly distributed over space and introduces additive noise to the images. Thermal noise cannot be avoided, but by adjusting the imaging parameters (TR, TE, flip angle, voxel size, receiver bandwidth) the signal intensity

can be increased.

System noise is caused by variations in the scanner hardware, such as static field inhomogeneity, nonlinearity in the gradient fields and off-resonance or loading effects in the transmitter and receiver coils. Changes in the static field can cause scanner drift over time, which affects the signal intensity. If the resonant frequency of the RF coils does not match the Larmor frequency of protons, the excitation will be imperfect, causing intensity variations in the MR images. Therefore, it is very important to conduct regular quality control checks for both the field homogeneity and the RF coils.

The most common and most disruptive noise sources in fMRI are subject motion and physiological artifacts, such as heart pulsation and breathing. Physiological signals are problematic because they occur at frequencies higher than the fMRI sampling rate. As a result, the cardiac and respiratory signals appear aliased in the BOLD signal. Prewhitening of the signal [Woolrich et al., 2001] is commonly used to correct for aliasing. Head motion during scanning causes variability in the fMRI time series. It can partly be eliminated by careful preprocessing, but large motion of more than one voxel size usually disrupts the data, making it unusable in the analyses. Motion is especially problematic if it is correlated with the experimental task. It is difficult to reduce even with signal processing and might lead to spurious interpretations about the brain activity. Therefore, it is easier to avoid motion artifacts than eliminate them after scanning. Careful planning of the experiment, supporting the subject's head with paddings during the measurement and instructing the subject to remain still are crucial for preventing unnecessary motion.

3.8 Preprocessing of fMRI data

Slice timing correction

Nowadays many fMRI studies use an interleaved slice acquisition protocol, in which the scanner first collects consecutively all odd-numbered slices and then even-numbered slices. The purpose of the interleaved acquisition is to avoid cross-slice excitations. However, this approach causes a time lag of TR/2 between the acquisition of the first and second slice. This results in different HRF estimations in consecutive slices, even if the hemodynamic response was nearly identical in them. Without correction, this time lag can severely violate the interpretation of the signal.

The correction for slice timing is done using temporal interpolation, which utilizes the signal from nearby time points to approximate the amplitude of the HRF in each slice. The middle time point of TR is typically used as a reference point. Sinc interpolation is commonly used for slice timing correction because of its capability to reduce noise-related variation in the signal.

Realignment

The purpose of volume coregistration is to minimize the artifacts caused by head motion. The realigmnent is performed by aligning a time series of successive volumes

into a single reference volume. A commonly used approach is a six-parameter rigid-body transformation, which assumes that the volume and shape of the brain are constant during imaging, and the only tranformations are translations along x-, y- and z-axes and rotations through the three imaging planes. Each volume is aligned to the reference volume by optimizing a cost function between the reference and the rigid-body transformed volume. There are several cost functions and algorithms available in the current fMRI processing software packages. Mutual information, which measures the mutual dependence of two random variables, is an example of a cost function that is maximized during realignment.

Coregistration

Functional MRI data are typically low resolution and lack contrast between anatomical structures. In order to account for these limitations, the functional volumes are coregistered by aligning them with each subject's high-resolution anatomical images. A six-parameter rigid-body transformation can be used if the contrasts of high- and low-resolution images are similar; in that case the optimal transformation is found by minimizing a cost function. However, if the contrasts are different in the two imaging modalities, algorithms based on mutual information should be used instead. In addition, if the functional images involve linear geometric distortions, it is appropriate to use a nine-parameter linear transformation, which includes three additional parameters for scaling differences along x-, y- and z-axes.

Spatial normalization

The anatomy and size of the brain vary largely between individuals. Despite that, the experimental studies usually have to involve a large number of subjects to achieve a sufficient statistical power. In order to compare the brain activity between subjects, their brains are normalized by a registration into a common space. The normalization minimizes the effects of anatomical differences by stretching, squeezing and warping the brain volumes until they match the reference volume. Usually a standard brain atlas is used as the common space; the most popular standard atlases are Talairach [Talairach and Tournoux, 1988] and Montreal Neurological Institute (MNI, [Evans et al., 1992]) atlases.

Spatial smoothing

Most fMRI analyses involve spatial filtering in order to decrease high-frequency spatial components and smooth the images. The filtering is useful, because the BOLD signal has spatial correlation between adjacent voxels due to functional similarity and vascular spreading of oxygenated hemoglobin. Activation at a single cortical area typically results in a signal increase in two or more voxels, indicating that the activity observed at a single voxel is not strictly located in that particular region. A filter that accounts for the spatial correlation of the signal can increase the SNR without a loss in spatial resolution. Another advantage of spatial filtering is that it reduces the probability for local intensity maxima, which further decreases the

number of false positives in the statistical activation analysis. In other words, if the data are spatially smoothed it is less likely that spurious activations in single voxels will be interpreted as significant activation changes, because the high signal intensity is spread over multiple voxels. The most common approach for spatial smoothing is a Gaussian filter, which distributes the intensity of a single voxel into nearby voxels using a normal distribution. The width of the Gaussian filter determines the distance of its effect, and it is expressed in millimeters at half of the maximum value (full width at half maximum, FWHM).

Temporal filtering

Temporal filtering is an important preprocessing step in the fMRI analysis, since aliasing and high-frequency noise can substantially reduce the signal quality. A low-pass filter with a cutoff at Nyquist frequency (1/2TR) will eliminate aliasing artifacts in the signal. Furthermore, physiological signals, such as heart pulsation and breathing, typically occur at higher frequencies than the BOLD signal and can thus be eliminated by low-pass filtering. However, in task paradigms with rapid presentation of stimuli these signals might have a similar frequency with the stimuli. Therefore, the filter parameters should be dependent on the experimental design. Very low-frequency (<0.01 Hz) noise, usually caused by the scanner drift, can be removed with a high-pass filter.

4 fMRI signal analysis

This chapter presents the concept of an event-related experimental design for fMRI. Also, we present two of the most popular signal analysis methods for fMRI: the general linear model (GLM) and independent component analysis (ICA). The general principles and mathematical formulations of both methods are overviewed, and their applicability for group-level studies is evaluated.

4.1 Event-related paradigms

An event-related fMRI design attempts to measure the BOLD responses related to transient stimuli. A trial consists of one or several events, and an event-related stimulus sequence typically involves tens or hundreds of trials. When the events are separated in time, the time-locked hemodynamic responses can be effectively averaged over trials; this method was originally applied to the event-related potentials (ERP) in EEG. Averaging over multiple trials emphasizes the event-related signal and attenuates the noise unrelated to the events. The segment of fMRI occurring time-locked to the onset of an event is called an epoch [Huettel et al., 2004], and it is assumed to contain the hemodynamic response associated with the event.

The interstimulus intervals (ISI) may range from seconds to tens of seconds, and nowadays a common approach is to use jittered time intervals between events. In the first studies using event-related fMRI, very long interstimulus intervals were used to prevent overlapping of individual BOLD responses. However, Dale and Buckner [1997] showed that by using a linear time invariant assumption about the BOLD signal, the responses can be robustly estimated for randomly intermixed events separated only by 2 seconds. Shortly after that, Bandettini and Cox [2000] estimated the optimal fixed ISI for a periodically presented 2 second stimuli to be 10–12 seconds, and showed that very short ISIs in periodic design deteriorate the detection of event-related responses. The reason for this is that the BOLD signal quickly saturates to its maximum value when stimuli are presented periodically. Using variable length ISIs this effect can be minimized. According to these findings, it is justified to use short, temporally jittered ISIs in event-related fMRI designs. Furthermore, randomization and counterbalancing of different events in an event sequence is important when the goal is to robustly elicit neural activation related to the different stimuli.

Event-related designs have several advantages compared to blocked paradigms. First, estimations for shape and timing of the hemodynamic responses are better in event-related designs, allowing for the accurate characterization of the waveform and latency of the HRF elicited by a certain stimulus. Second, the event-related design is more feasible for studying specialized brain functions, since different aspects of the stimuli, such as faces, colors and buildings in a photograph, can be separately modelled. If the events are sorted according to one of the features and a corresponding explanatory variable is constructed, brain responses evoked by that particular feature can be detected. However, the blocked designs generally have a better detection power for brain activity than the event-related designs. This dis-

advantage can partly be overcome by increasing the number of events, but since the percent signal change in event-related BOLD responses is much lower (<1%) than the change elicited by continuous block stimuli (2–3 %), the statistical power in the event-related paradigms remains poor [Huettel et al., 2004].

4.2 General linear model

The conventional approach for mapping stimulus-related activations in fMRI is to construct one or several regressors for the general linear model (GLM) and statistically fit their linear combination into the BOLD signal of each individual voxel. This procedure is referred to as statistical parametric mapping (SPM, [Friston et al., 1994]). The model for a response variable (i.e. HRF at at given voxel) can be expressed as:

$$x_{ij} = g_{i1}\beta_{1j} + g_{i2}\beta_{2j} + ... + g_{iK}\beta_{Kj} + e_{ij} \tag{10}$$

where i denotes the number of a scan and j the number of a voxel. Explanatory variables g_{ik} are related to the measurement conditions and can be either covariates, such as the global signal change and the scanner noise, or indicator variables, such as the stimulus time courses convolved with the standard HRF. The values β_{Kj} are the parameters to be estimated. They can be interpreted as weights representing the contribution of each explanatory variable to the variation of the total signal. Signal errors e_{ij} are assumed to be statistically independent and identically normally distributed.

Equation (10) can be written in a matrix form:

$$\mathbf{X} = \mathbf{G}\beta + \epsilon \tag{11}$$

where $\mathbf{X}$ contains the measured fMRI data (one column for each voxel, one row for each scan), $\mathbf{G}$ is the design matrix containing the regressors (one column for each explanatory variable, one row for each scan) and ϵ contains the normally distributed error terms.

The model is fitted to the data by ordinary least squares estimates b for β. These estimates satisfy the normal equations:

$$\mathbf{G^T G b} = \mathbf{G^T X} \tag{12}$$

If $\mathbf{G}$ has a full rank the least squares estimates are uniquely defined as

$$\mathbf{b} = (\mathbf{G^T G})^{-1}\mathbf{G^T X} \tag{13}$$

Since the parameter estimates are normally distributed and the error term can be determined, it is possible to infer if the model $\mathbf{b}$ for the activation differs significantly from the null hypothesis, which is tested by t-statistics. A significant p-value in a given voxel indicates that the voxel BOLD signal is significantly modulated by the model waveform.

The design matrix may include one or several experimental conditions as columns. By contrasting the parameter estimates of different regressors it is possible to infer

the difference between task and baseline or between two tasks. In the latter case, the regressors corresponding to different conditions must have opposite signs. GLM can be extended to a group level using individual parameter contrast maps in a random- or mixed-effects analysis, which estimates significant activations averaged over the group.

GLM is an efficient approach for most block designs and simple event-related designs, as it is possible to include the stimulus parameters and additional noise into the model. However, in more complicated designs GLM is insufficient for modeling the produced neural activations. For example, in many naturalistic paradigms the model does not have a unique form or the responses cannot be reliably predicted, which makes the construction of the regressors very difficult or even impossible.

4.2.1 FIR and other convolution models for HRF

Convolution models estimate the BOLD signal by a hemodynamic response function (HRF). The shape of a typical canonical HRF is shown in Fig. 5. Individual responses to two transient stimuli are linearly summated when the stimuli are presented with a short interstimulus interval. The responses peak approximately 4–5 s after stimuli and the undershoot lasts up to 30 s post-stimulus. A continuous 10–s stimulation causes an HRF with a similar shape, but a longer duration of peak activation. An initial undershoot of the HRF is not shown here, although some models include it.

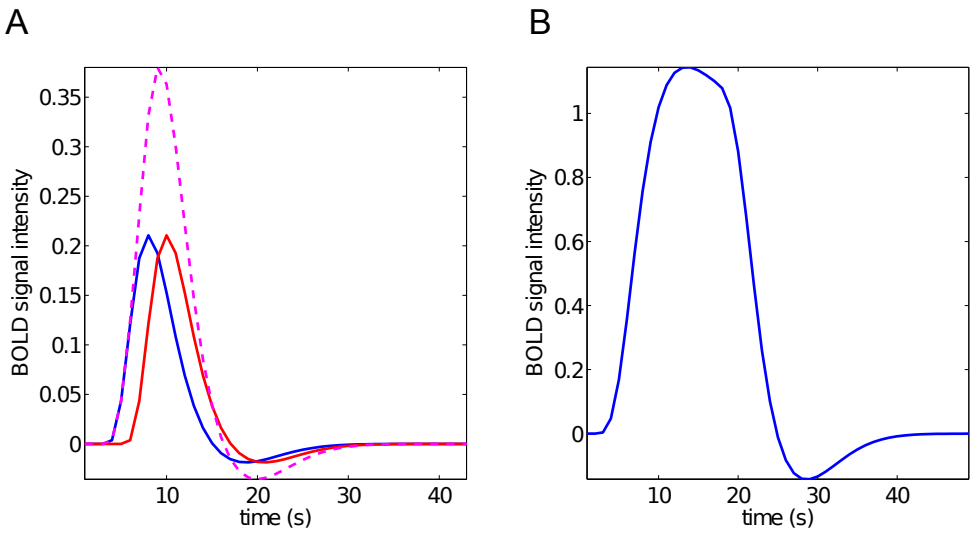

Figure 5: A) Canonical hemodynamic responses elicited by two transient stimuli 1 and 2 (solid lines), and the linear sum of their responses (dashed line). B) A canonical hemodynamic response resulting from 10 seconds of continuous stimulation.

When multiple stimuli are presented in a rapid succession, their responses overlap and are expected to add up linearly. Therefore, the BOLD signal can be modelled as an output of a linear time-invariant system, stating that the HRF caused by a transient stimulus has a finite duration and is independent of time. The BOLD time course can be expressed as a convolution of the stimulus function $u(t)$ with the HRF estimate $h(\tau)$:

$$X(t) = u(t) \times h(\tau) = \int_0^T u(t-\tau)h(\tau)d\tau \tag{14}$$

where τ is the estimated time window of the BOLD response. Stimulus function is a stick (or boxcar) function indicating the onsets (and offsets) of stimuli. The strength of the stimuli can be included in the functions by parametric modulation, i.e. weighting the stick functions with appropriate magnitudes before the convolution.

As the shape of the HRF varies over individuals and brain regions, the convolution model has to include some flexibility to account for this variation. The easiest approach is to use temporal basis functions $f_k(\tau)$ in the model HRF. Basis functions express the complicated signal as a linear combination of simple functions:

$$h(\tau) = \sum_{k=1}^{K} \beta_k f_k(\tau) \tag{15}$$

The neural activation resulting from the stimuli can be expressed as a series of J impulses at times o_j, and the stimulus function is:

$$u(t) = \sum_{j=1}^{J} \alpha_j \delta(t - o_j) \tag{16}$$

where α_j includes the parametric modulations of the stimuli and $\delta(t)$ is the Dirac delta function. The convolution of the two previous functions gives the following GLM equation:

$$y(t) = \sum_{j=1}^{J} \sum_{k=1}^{K} \beta_k f_k(t - o_j) + \epsilon(t) \tag{17}$$

where β_k represent the parameters to be estimated.

There are several sets of basis functions. The most flexible basis sets are finite impulse response (FIR) and Fourier sets, which do not make any *a priori* assumptions about the shape of the HRF. The FIR basis set contains a series of contiguous timebins, which produce the averaged HRF in each post-stimulus timebin, corresponding to the parameter estimates [Henson et al., 2001]. The FIR model can detect responses of any shape within the given temporal window. The Fourier set consists of a constant term and multiple sine and cosine functions, and it is able to capture any response within a predefined frequency range. A slightly more constrained basis set is the set of gamma functions, which includes several possible

HRFs with different phase delays. Using gamma functions requires fewer basis functions, because the model makes initial assumptions about the shape of the HRF. It is also possible to use a basis set including the canonical HRF and its partial derivatives [Henson et al., 2001]. However, when in doubt about the shape of the HRF or the location of activated brain regions, more general basis sets should be used. In particular, when modelling the neuronal activations corresponding to complex stimuli, flexible HRF models are useful, since there is probably high variability in the responses across brain regions. In this study we modelled the BOLD responses with FIR basis functions.

When the convolution model has been determined, the design matrix for the GLM can be constructed. Each basis function is represented as a separate regressor in the design matrix. Contrasts between different stimulus conditions can be modelled by setting appropriate weights for the corresponding regressors. For example, if the purpose is to examine the difference in activity between task A and task B, the corresponding regressors should have weights 1 and -1, respectively. Additional variables, such as motion parameters and the mean signal, can also be included in the design matrix. If it is assumed that different stimuli are correlated, the corresponding regressors should be orthogonalized such that they do not share any common signal. Motion parameters and other additional explanatory variables should always be orthogonalized with respect to the stimulus variables.

4.3 Independent component analysis

Independent component analysis (ICA) is a non-parametric signal analysis method commonly applied to fMRI data in order to extract spatially and temporally separate components from the measured voxel-wise signals. Under the assumption that the signals are linear combinations of statistically independent source signals, ICA attempts to decompose the original signal into the source components [Hyvärinen and Oja, 2000]. Two widely used algorithms for performing ICA are FastICA [Hyvärinen and Oja, 2000] and Infomax [Bell and Sejnowski, 1995]. Each algorithm uses slightly different nongaussianity measures and parameter estimations.

4.3.1 Estimating statistical independence

The ICA model consists of the measured signals $\mathbf{x}$, the mixing matrix $\mathbf{A}$ and the source signals $\mathbf{s}$, and can be expressed in a matrix form:

$$\mathbf{x} = \mathbf{A}\mathbf{s} \tag{18}$$

A major problem in this model is that both $\mathbf{A}$ and $\mathbf{s}$ are usually unknown. Therefore, $\mathbf{A}$ has to be estimated in order to find $\mathbf{s}$. Thereafter, the components can be solved using the inverse matrix $\mathbf{W} = \mathbf{A}^{-1}$:

$$\mathbf{s} = \mathbf{W}\mathbf{x} \tag{19}$$

The ICA model involves two ambiguities. First, the signs and scales of the independent components cannot be determined, i.e. multiplying the components by

any scalar variable does not affect the results. Second, the order of the components cannot be determined, as the order of the terms in the linear sum can be freely changed.

A fundamental requirement for estimating the ICA model is nongaussianity of the source components. Most ICA algorithms attempt to maximize an objective function estimating nongaussianity. Examples of nongaussianity measures are kurtosis and negentropy. Kurtosis measures the peakedness of a statistical distribution and is defined as:

$$kurt(s) = E\{s^4\} - 3E\{s^2\}^2 \tag{20}$$

For Gaussian distributions, kurtosis equals to zero. Kurtosis is easy to compute, but it is not a very robust method, since it is sensitive to outliers in the data. Negentropy (negative entropy) is based on the measure of entropy H, which describes the uncertainty of the data. Since gaussian distributions are highly predictable and thus tend to have a high entropy, maximizing nongaussianity is equal to minimizing entropy. Negentropy, or differential entropy, is defined by:

$$J(s) = H(s_{gauss}) - H(s) \tag{21}$$

where s_{gauss} is a random Gaussian variable having the same covariance matrix with s. Negentropy is non-negative and zero if and only if s is Gaussian. Negentropy is a well-defined quantity in terms of the statistical theory, but it is very difficult to compute. Therefore, in practice some approximations of negentropy are used.

Besides estimating nongaussianity, independence can be validated by minimizing mutual information. Mutual information I is a measure of dependence between random variables and it is defined as:

$$I(s_1, s_2, ...s_n) = \sum_{i=1}^{m} H(s_i) - H(s) \tag{22}$$

Mutual information is always non-negative, and zero if and only if the variables y_i are statistically independent. Minimizing mutual information is equivalent to maximizing nongaussianity of the variables.

4.3.2 Data preprocessing for ICA

It is usually necessary to perform certain preprocessing steps before performing ICA. First, the data is centered by subtracting the mean. Second, the data is whitened, i.e. vector $\mathbf{x}$ is transformed such that its components are uncorrelated and have a unit variance. The whitening transformation can be done using the eigenvalue decomposition of the covariance matrix $\mathbf{Exx^T}$=$\mathbf{EDE^T}$, where $\mathbf{E}$ is the eigenvector matrix and $\mathbf{D}$ a diagonal matrix containing the eigenvalues of $\mathbf{xx^T}$. The whitened vector is thus obtained by

$$\widetilde{\mathbf{x}} = \mathbf{ED^{-1/2}E^Tx} \tag{23}$$

The whitened ICA model becomes

$$\widetilde{\mathbf{x}} = \mathbf{E}\mathbf{D}^{-\mathbf{1/2}}\mathbf{E}^{\mathbf{T}}\mathbf{A}\mathbf{s} = \widetilde{\mathbf{A}}\mathbf{s} \tag{24}$$

The white mixing matrix $\widetilde{A}$ is orthogonal and contains only $n(n-1)/2$ degrees of freedom, compared to n^2 in the original mixing matrix. Therefore, the whitening substantially reduces the number of independent components and decreases the complexity of the problem. Furthermore, it is useful to do a dimension reduction by principal component analysis (PCA) in parallel with the whitening. PCA can be used to estimate the eigenvalues of $\mathbf{E}\mathbf{x}\mathbf{x}^{\mathbf{T}}$ and preserve only the largest ones, on which the data is then projected. Reducing dimensions usually diminishes noise and prevents overfitting [Hyvärinen and Oja, 2000], which can be a problem with large data dimensions.

4.3.3 Group ICA

ICA cannot be generalized to a group level in a straightforward way, as the voxel time courses are different for individual subjects. However, [Calhoun et al., 2001] introduced a method for performing group ICA, and used it to separate spatial components in fMRI data. The method consists of data reduction, ICA and component back reconstruction. In the data reduction step, PCA is used to reduce dimensions. First each subject's functional data is reduced by PCA. After that, all subjects are concatenated into a single group and the data reduction is performed again in a group level. ICA is applied to the reduced dataset in order to find independent components for the whole group. In the back reconstruction step, individual subjects' components are calculated using aggregate group ICA components and the results from data reduction for each subject. ICs of individual subjects are used for calculating the group statistics, such as t-statistics and mean values, and the resulting statistical maps are thresholded for visualizing meaningful components. Component time courses can additionally be fitted to the stimulus model to find stimulus-related components.

5 Materials and methods

5.1 Subjects

Twenty-two healthy volunteers (21–50 years, mean 25.5 years, 10 females and 12 males) participated in the study. The subjects reported no current neurological or psychiatric diseases or medication affecting the central nervous system. In addition, all subjects had normal or corrected-to-normal vision. Permission for the study was acquired from the ethical committee of Aalto University. The study was carried out in accordance with the guidelines of the declaration of Helsinki, and informed written consent was obtained from each subject prior to scanning. The subjects were paid 20 e/h for participating. One subject was unable to complete the scan due to an uncomfortable sensation felt inside the scanner and was excluded from the analysis.

5.2 Stimuli and experimental procedures

The experiment consisted of three tasks, presented in the same order for all subjects. None of the tasks included auditory stimuli. In the first task the subjects played a simple video game by pressing buttons with their both index fingers. The game scene included a background picture of a garden and two holes on both sides of the screen. Two cartoon characters, a rabbit and a mole, appeared from either of the holes one at a time in a pseudo-random sequence. The participants were instructed to whack the mole with a club by pressing the button on the side where the mole appeared, and avoid hitting the rabbit by whacking the empty hole on the opposite side when the rabbit emerged. Whacking the rabbit and failing to whack the mole were considered errors, as well as not reacting within 700 ms while the cartoon characters appeared on the screen. Subjects received visual feedback (green "%" indicating success and red "X" indicating error) on the screen after each trial. The total trial duration was 2 s, consisting of the stimulus (up to the reaction time, max 700 ms), response (200 ms), feedback (500 ms) and null time up to 2 s. Intertrial intervals were pseudo-randomly jittered to 0, 1, 2, 3, 4 or 5 s, average ITI being 1.86 s. The total duration of the game was approximately 15 minutes. Timings for error and success trials were collected during the game from each subject.

In the second task the subjects passively watched a 15–minute video recording of the previously described game. The video only presented the game as it appeared on the screen, i.e. the player was not visible. The task was to observe errors occurring in the game; the video included 26 errors in total. The visual appearance and the timing of the stimuli were identical to the first task, but the subjects were not supposed not press any buttons during the observation task.

In the third task the subjects watched short video clips depicting errors in naturalistic situations, such as figure skaters falling down, people slipping on an icy street and someone accidentally hitting a wrong person in the face. The concept of 'error' in this paradigm was quite wide; we defined errors generally as failures to achieve current goals. The video included 35 errors in total. Because we wanted

to ensure that the subjects did not expect errors to occur in every video clip, the video also included clips containing successful performance. The order of 'success' and 'error' clips was randomized. The total duration of the video was 19 minutes 20 seconds.

The stimuli were controlled using Presentation software (Neurobehavioral Systems Inc., Albany, California, USA) and projected on a semi-transparent screen behind the subject's head via a 3–micromirror data projector (Christie X3, Christie Digital Systems Ltd., Mönchengladbach, Germany). Image width was 28 cm and the distance to the screen 34 cm from a mirror above the subject's eyes. LUMItouchTM fMRI optical response system was used as the response device, and the subjects had a keypad with one active response button on each hand. The subjects had earplugs for hearing protection and foam paddings on both sides of their head to suppress head movement. They were instructed to avoid moving during the scan.

5.3 Data acquisition

The fMRI scanning was conducted in the Advanced Magnetic Imaging (AMI) Centre of the Aalto University School of Science. BOLD fMRI was performed with a 3.0 T Siemens Magnetom Skyra MRI scanner (Siemens Healthcare, Erlangen, Germany) using a 30-channel head coil and a standard T2* weighted EPI sequence. The imaging area consisted of 32 whole-brain functional gradient echo echo-planar oblique slices (slice thickness 4.5 mm, in-plane resolution 3.5 mm x 3.5 mm, field of view (FOV) 224 x 224, voxel matrix 64 x 64, TE 30 ms, TR 2000 ms, flip angle 75°). The slices were acquired in an ascending interleaved order. In addition, anatomical whole-brain T1 images with 176 oblique slices were acquired using a magnetization prepared rapid acquisition gradient echo (MPRAGE) sequence (TR 2530 ms, TE 3.3 ms, TI 1100 ms, flip angle 7°, slice thickness 1.0 mm, FOV 256 x 256).

5.4 Preprocessing

Functional Magnetic Resonance Imaging of the Brain Centre (FMRIB) software library (FSL, release 5.0; www.fmrib.ox.ac.uk/fsl; [Smith et al., 2004]) was used to preprocess the fMRI data. First three volumes of each run, corresponding to the presentation of the instruction trials, were removed in order to account for T1 stabilization. Slice timing was corrected with FSL's sinc interpolation using the middle slice as a reference. Motion parameters were extracted with Motion Correction using FMRIB's Linear Image Registration tool (MCFLIRT; [Jenkinson et al., 2002]. Runs with more than 2.0 mm replacement, 2.0 mm translation or 2° rotation were discarded from further analyses. As a result, the final datasets included data from 18 subjects in the game playing task, 19 subjects in the game observation task and 18 subjects in the naturalistic task.

Non-brain matter was removed from both anatomical and functional images using Brain Extraction Tool (BET; [Smith, 2002]). The intensity threshold and threshold gradient in BET were manually adjusted and the anatomical images were visually inspected to achieve optimal brain extraction results. The signals were

temporally high pass filtered with Gaussian-weighted least-squares straight line fitting and sigma = 100 s. The volumes were spatially smoothed with a 8.0 mm FWHM Gaussian kernel. Functional images were registered with FMRIB's Linear Image Registration tool (FLIRT; [Jenkinson et al., 2002]) to the brain extracted T1 weighted images of each subject using 9 degrees of freedom (DOF). This data were further registered into FSL's 2.0 mm MNI152 standard space template using 9 DOF. The signals in each voxel were prewhitened with FMRIB's Improved Linear Model (FILM) to eliminate autocorrelation and obtain maximal detection efficiency. Finally, motion parameters obtained from MCFLIRT were used to regress motion artifacts out of the data.

5.5 Statistical analyses

5.5.1 GLM

The GLM analysis was performed with FSL's FMRI Expert Analysis Tool (FEAT). FIR estimates of the event-related hemodynamic responses were calculated for errors and successful trials in the game playing and game observation tasks. The FIR model included five contiguous basis functions, each having a duration of one TR (2 s). We did not use any orthogonalization of the regressors, as the random jittering of the stimuli ensured that there was no significant correlation between them. An example of a design matrix is presented in Fig. 6.

The model was fitted to each voxel's signal using ordinary least squares estimation. As a result, the average signal intensity at the five post-stimulus time points was obtained. Five parameter estimates were calculated corresponding to the significance of activity at each post-error time point. In addition to the parameter estimates for errors and correct trials, contrasts for error vs. correct and correct vs. error were calculated for both self-committed and observed game conditions in order to eliminate confounding factors, such as the activity caused by button presses.

Before constructing the design matrices for the naturalistic paradigm, we collected subjective ratings about the video attributes from the participants. The ratings were collected after scanning, since it was assumed that reviewing the video clips would not substantially affect the subjective responses to them. In-house software was used to collect ratings for 1) the intensity of error, 2) error anticipation, 3) amount of pain in the video clips. Ratings for each attribute were collected on separate runs. The subjects watched the video clips on a computer screen and gave ratings continuously by moving a cursor up and down on the edge of the screen. Ratings were collected at 5 Hz using a scale from 0 (no error/prediction of error/pain) to 1 (very intense error/high prediction of error/very intense pain). We included ratings for pain in the analyses because it is commonly acknowledged that many regions contributing to error processing, including dACC and insula, also respond to observed pain in other people [Jackson et al., 2005; Lloyd et al., 2004]. Therefore, the pain rating was used as a confounding regressor when examining the responses to errors.

The event-related design matrices were constructed using individual ratings as

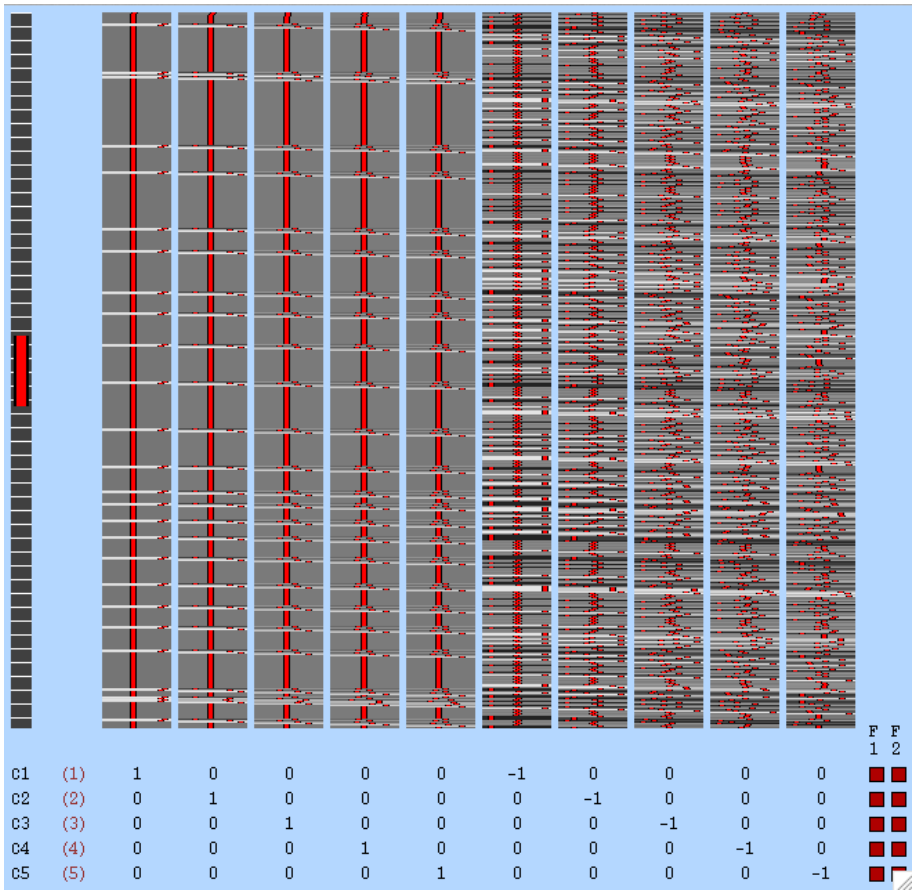

Figure 6: An individual subject's design matrix used in the GLM analysis of the game playing task. Errors and correct trials are represented by the first and last five regressors, respectively. The errors have a positive sign and the correct trials a negative sign, corresponding to the error>correct contrast.

parametric modulators of the regressor functions. The rating time series were first downsampled to match the TR of 2 s. Next, the ratings were normalized to Z scores and averaged over subjects. In the cases of error and pain ratings, the regressor time courses were set to the average value of ratings at time points which were manually labeled as error onsets, and zero elsewhere. In the case of error anticipation, time points on which the average rating exceeded 0.5 were included in the design matrix as 'anticipation events'. The regressors were convoluted with a FIR set including five contiguous basis functions. For each subject, activation maps were constructed corresponding to the following contrasts: error vs. baseline, error vs. anticipation, anticipation vs. baseline and error vs. pain.

In the group-level analysis, individual contrast estimates were subjected into a mixed-effects model using FMRIB's Local Analysis of Mixed Effects (FLAME) to detect the mean group effect. Z (Gaussianised T/F) statistic images were thresholded using clusters determined by Z>2.3 and a corrected cluster significance threshold of p=0.05, using Gaussian Random Field theory [Worsley et al., 2004]. Similar thresholds were used when contrasting activations between different conditions in a group level.

For visualization of the results, the statistical maps were projected onto an average cortical surface with the use of multifiducial mapping using CARET software [Van Essen, 2005]. Transverse slices were constructed with MRIcron ([Rorden et al., 2007], http://www.mccauslandcenter.sc.edu/mricro/mricron/) by overlaying the activation maps on the standard template brain.

5.5.2 ROI-based analyses

Spherical (6 mm radius) regions of interest (ROIs) were constructed around 23 voxels showing significant activation in one or several error conditions. Because we were especially interested in striatal activation, subregions of the striatum (putamen, globus pallidus and caudate nucleus) were defined as separate ROIs in the analyses. All ROIs, except the medial frontal cortex, were defined in both hemispheres separately for examining the effect of lateralization.

Percent signal change was calculated within the predefined ROIs for each subject in a time window spanning 10 s post-error. Mean signal change and standard error of the mean (SEM) at 4 s were calculated for both errors and correct trials. Error-related BOLD responses were compared between different conditions to find out which ROIs showed significantly ($p<0.05$, FDR corrected) different responses. In addition, the correlations of BOLD responses between all pairs of ROIs were calculated within a 10 s time window. The correlation coefficients were first calculated individually for each subject and then averaged using Fisher's Z transform [Corey et al., 1998] to account for a skewed sampling distribution.

5.5.3 ICA

ICA was performed with GroupICA of fMRI toolbox (GIFT, http://icatb.sourceforge.net/groupica.htm). Using the Minimum Description Length

(MDL) algorithm implemented in GIFT, the optimal numbers of components corresponding to game playing, game observation and naturalistic tasks were determined to be 115, 129 and 141, respectively. However, running GroupICA with these dimensionalities yielded very unstable component estimates, probably due to overfitting [Hyvärinen and Oja, 2000]. Therefore, the final number of ICs was selected *post hoc* by repeating the bootstrap calculation with several dimensionalities. In the game playing and game observation conditions the most stable estimates were obtained with 20 components, and in the naturalistic condition with 25 components.

Two data reduction steps were performed with expectation maximization PCA prior to running GroupICA. In the first step, data from each subject and dataset were reduced to the optimal number of dimensions given by MDL. In the second reduction step, the compressed data for each subject were concatenated with each other and reduced again into the most stable numbers of components. The procedure was performed for each dataset separately.

ICA was applied to the reduced datasets using FastICA algorithm. Group ICA was performed 20 times with random initialization and bootstrapping implemented in the ICASSO package in GIFT. The resulting components represented the most robust estimates obtained with multiple ICASSO runs. All components shown in the results had a robustness index of higher than 0.9. The components were finally back-reconstructed into individual subject maps using GICA3 algorithm. However, group statistics (mean, standard deviation and t-maps) were calculated over the number of subjects. The group average maps were visually inspected to discard ICs primarily containing artifacts, such as signal from white matter, signal from ventricles or residual motion. The resulting arbitrary component time courses and spatial maps were scaled to Z-scores. The spatial maps for each IC represented the strength of the component on each brain region, high Z-scores indicating a strong regional contribution to the component time course.

The resulting group-level ICs were subjected to a multiple regression analysis in order to detect error-related components, following the procedure presented in [Kim et al., 2009]. The stimulus functions were similar to the ones used in the GLM analysis, i.e. included ones at the event onsets and zeros elsewhere. The design matrices were constructed by convoluting the stimulus functions with a standard canonical HRF implemented in SPM5. The component time courses were first sorted according to the regression coefficients. After that, a multiple regression analysis was carried out to obtain a set of beta weights for each subject and regressor. In the game playing and game observation conditions, the beta weights were then subjected to a one-way analysis of variance with respect to the regressors in order to determine how much each time course was modulated by errors relative to correct trials. In the naturalistic condition, the contrast was made between errors and a baseline constant. In addition, one-sample t-tests were performed separately to all components and regressors against the null hypothesis of no event-related signal change.

6 Results

6.1 Behavioral performance

The subjects made 48.56 errors on average (SEM 5.66) in the game playing task. All subjects made ten or more errors, which was required for reliable averaging of the event-related BOLD response.

6.2 GLM

6.2.1 Error-related activation in different conditions

Robust BOLD responses were elicited in several cortical and subcortical brain regions by self-committed errors and observed naturalistic errors. The FIR model revealed that the peak of the BOLD response occurred 4 s after errors in these two conditions. Self-committed errors elicited significant activation in dACC, medial frontal cortex, bilateral insula, bilateral putamen, red nucleus, visual cortex and inferior temporal cortex at 4 s. The Z-statistical maps representing significant ($Z>2.3$, cluster threshold $p<0.05$) error-related activation in the self-committed condition at 4 s are presented in figure 7. Also when contrasted with correct responses, self-committed errors produced increased activity in dACC, bilateral insula, medial frontal cortex, putamen and superior temporal gyri at 4 s. However, correct trials elicited increased activity in bilateral putamen and medial orbitofrontal cortex at 6 s. The activation maps corresponding to the contrasts between errors and correct trials are presented in Fig. 8.

Naturalistic observed errors caused significant activity in bilateral middle temporal gyri, medial frontal gyrus, visual cortex (mostly in lingual gyrus) and cerebellum. The Z-statistical maps representing significant ($Z>2.3$, cluster threshold $p<0.05$) error-related activation in the naturalistic condition at 4 s are presented in figure 7. When the effect of pain observation was regressed out, additional activation foci were detected in rACC and right angular gyrus at 4 s. The corresponding Z-statistical activation map is presented in Fig. 9.

Observed game errors produced significant activity in right middle temporal gyrus, right inferior frontal gyrus, left superior and inferior parietal lobules and bilateral fusiform gyrus at 4 s. The contrast between errors and correct responses showed significant activity only in the right inferior frontal gyrus at 4 s. The activation maps corresponding to the contrasts between errors and correct trials at 4 s are presented in Fig. 8. At 2 s this contrast showed activity in bilateral inferior frontal gyri and bilateral middle temporal cortices as well. However, considering that the latency of BOLD response is typically 4-5 seconds, this activity was most likely insignificant noise and therefore not shown.

The tables corresponding to all aforementioned activation maps are shown in Appendix A.

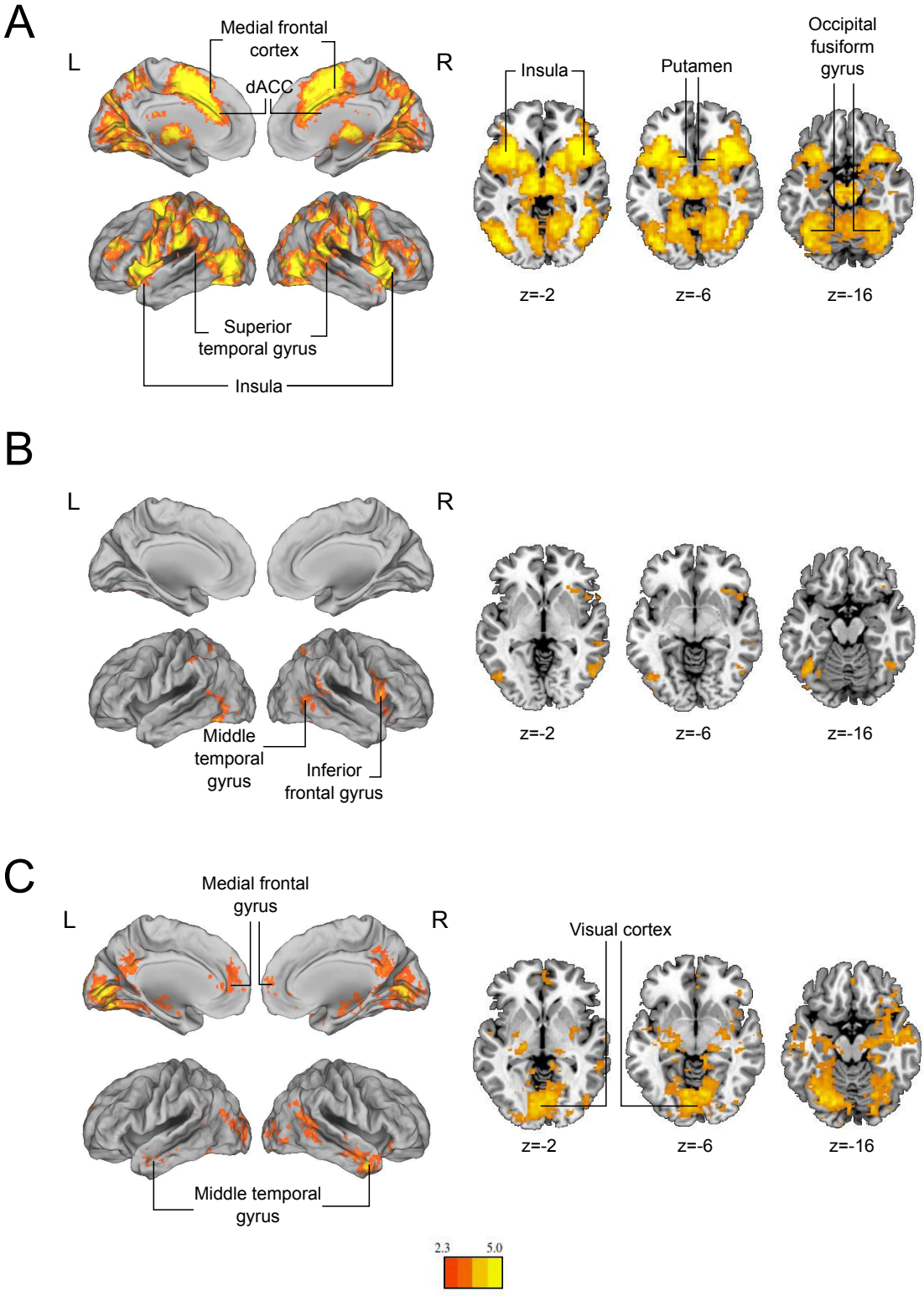

Figure 7: *Z*-statistical maps of error-related activations 4 s after A) self-committed errors, B) observed game errors, C) observed naturalistic errors.

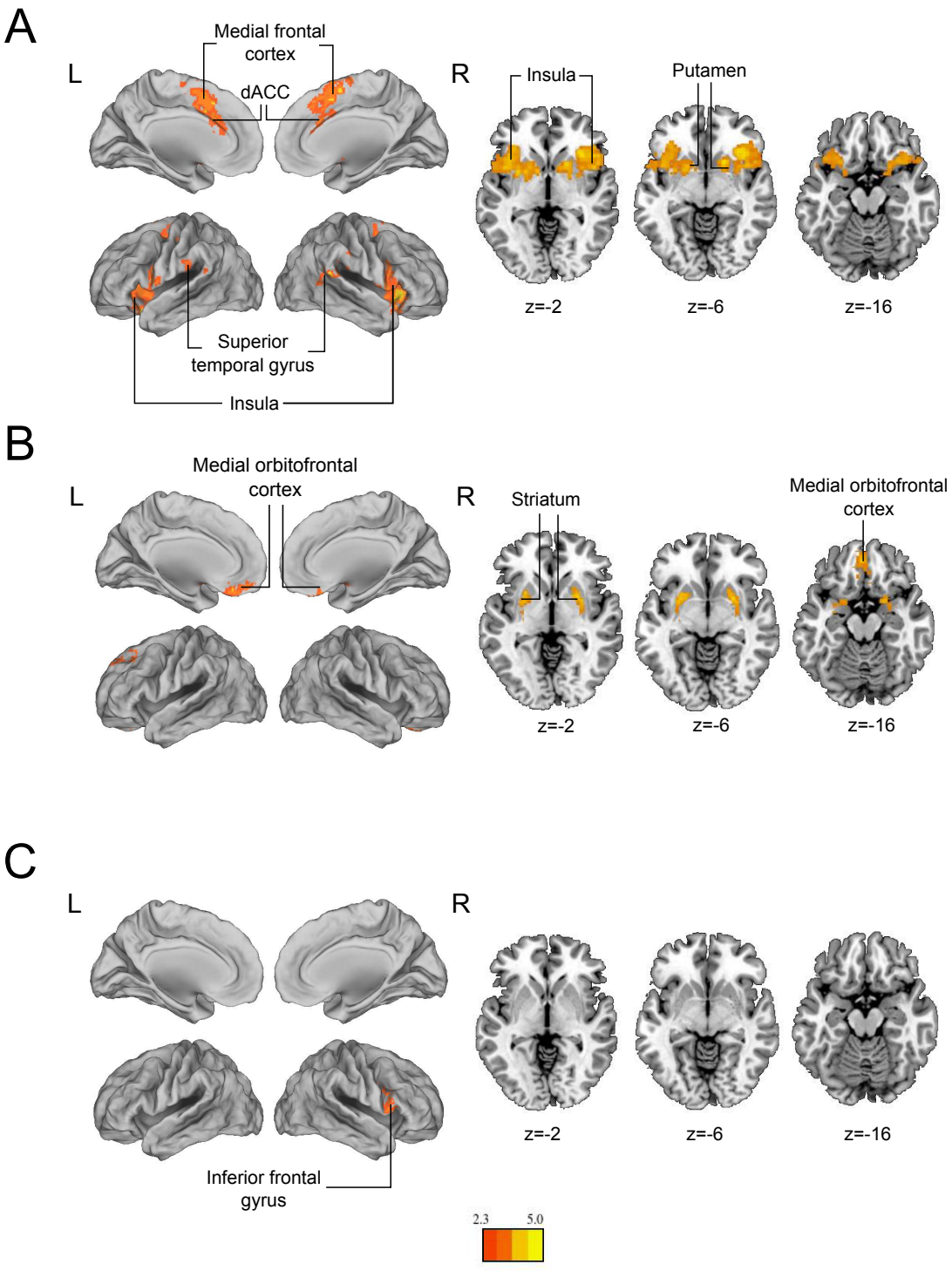

Figure 8: Z-statistical maps of contrasts for A) error>correct at 4 s in self-committed condition, B) correct>error at 6 s in self-committed condition, C) error>correct at 4 s in observed game condition.

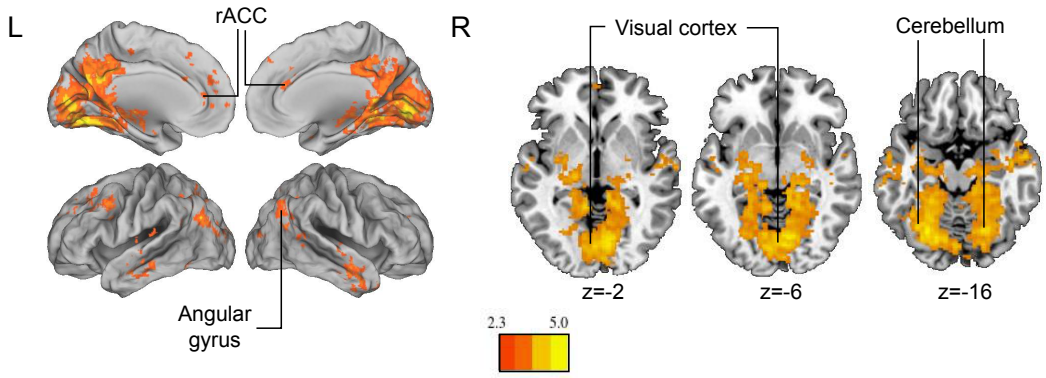

Figure 9: Z-statistical maps of error-related activations at 4 s in the naturalistic condition with the effect of pain regressed out.

6.2.2 Differences between experimental conditions

There were certain significant differences in the error-related activation patterns corresponding to the different conditions. Self-committed errors, compared to observed game errors, caused higher activity in dACC, medial frontal cortex, insula, putamen, cuneus and visual cortex, but observed game errors did not cause increased activity in any brain region. Naturalistic errors, compared to observed game errors, produced increased activity in rACC, anterior medial frontal cortex and visual cortex, whereas observed game errors caused increased activity in right inferior frontal gyrus and left superior parietal lobule. Self-committed errors, compared to naturalistic errors, caused more significant activity in dACC, insula, red nucleus, right inferior temporal gyrus and right middle frontal gyrus, whereas naturalistic errors caused increased activity in posterior cingulate, superior frontal gyrus and superior temporal gyrus. The Z-statistic maps representing pairwise differences between conditions are shown in Fig. 10, and the corresponding tables in Appendix A.

6.2.3 Effect of error anticipation

Error anticipation in the naturalistic task elicited significant activation in bilateral insula and striatum, as well as in dorsal ACC and supplementary motor area. In addition, activity during error anticipation was increased in the aforementioned regions and additionally in precentral gyrus, when contrasted with error occurrence (2 s from the maximum of anticipation vs. 2 s from error). Error occurrence, contrasted with error anticipation, caused increased activity in rACC and visual cortex (4 s from the maximum of anticipation vs. 4 s from error). Unexpected errors caused increased activation in the rACC, whereas anticipated errors elicited activity specifically in the occipital visual areas. Z-statistical maps of contrasts representing anticipation vs. baseline, anticipation vs. error and anticipated vs. surprising errors are shown in Fig. 11. The corresponding tables of activation clusters are shown in Appendix A.

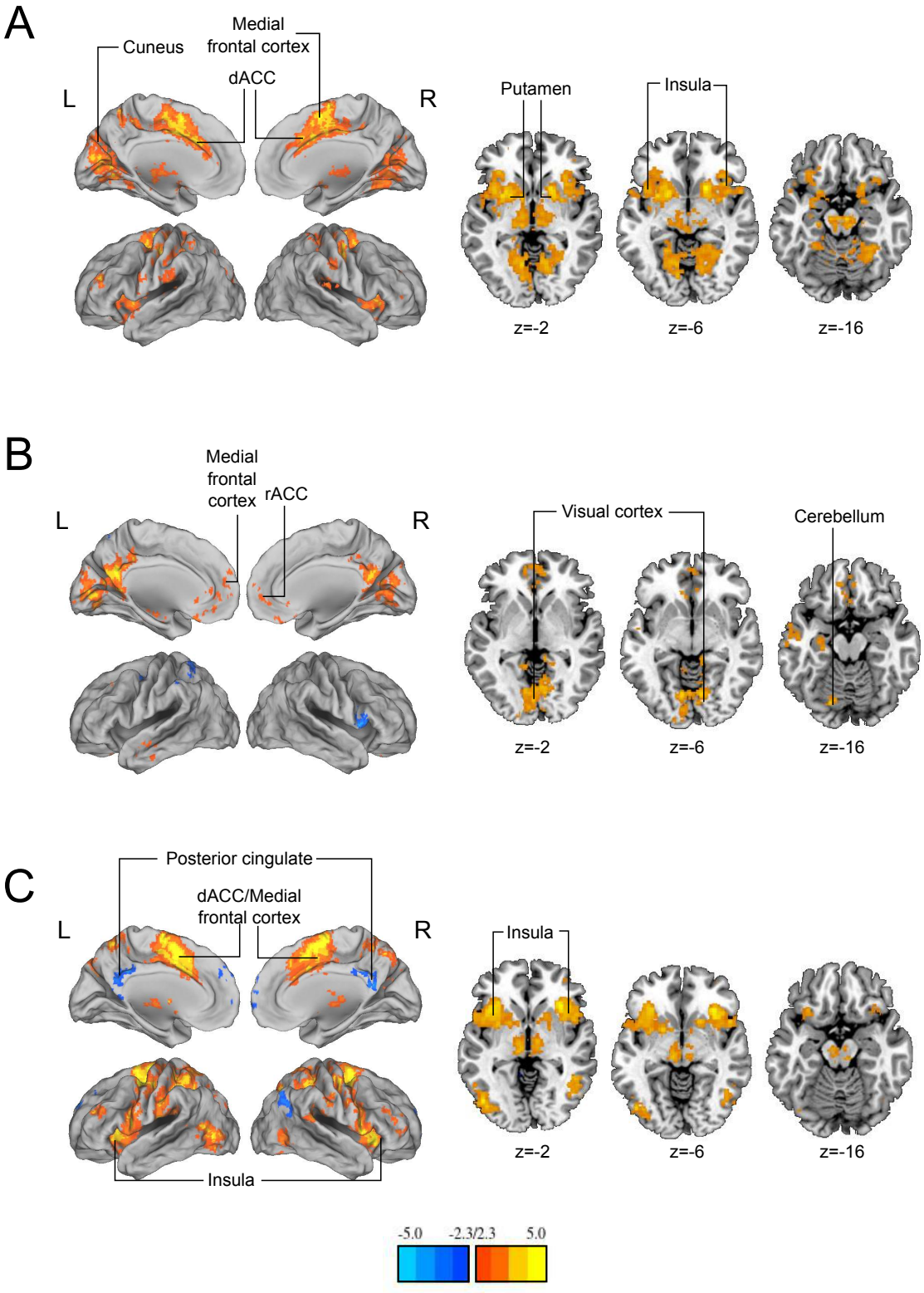

Figure 10: *Z*-statistical maps of differences between activations at 4 s. A) self-committed (red-yellow) vs. observed game (blue-cyan), B) naturalistic (red-yellow) vs. observed game (blue-cyan), C) self-committed (red-yellow) vs. naturalistic (blue-cyan).

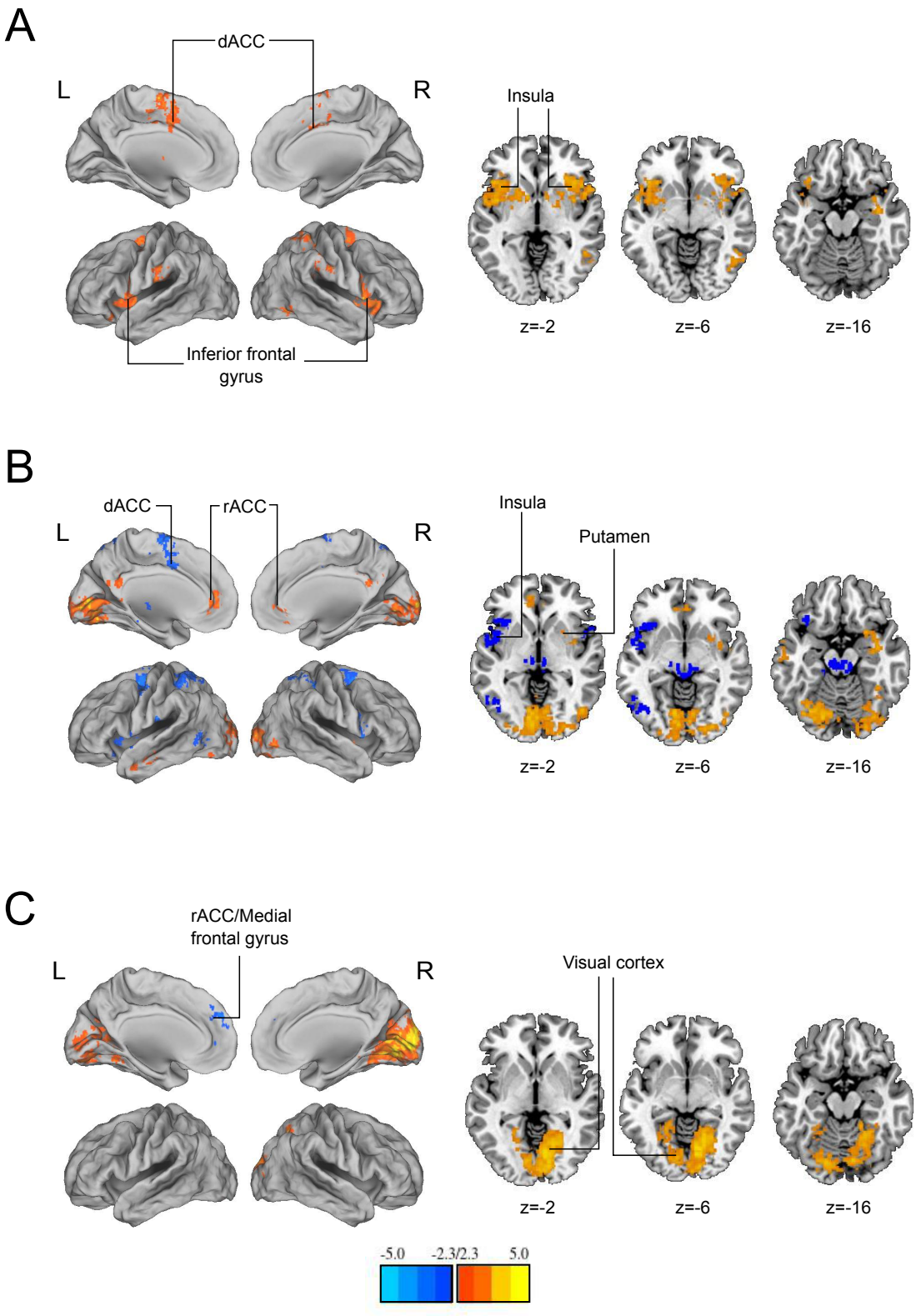

Figure 11: Z-statistical maps for A) error anticipation (2 s from maximum anticipation), B) contrasts between error occurrence (red-yellow) and error anticipation (blue-cyan), C) contrasts between anticipated errors (red-yellow) and surprising errors (blue-cyan).

6.3 ROI-based analyses

The correlations between ROIs differed across conditions. In general, the highest correlation values were obtained during self-committed errors. Naturalistic errors resulted in slightly higher between-region correlation values than observed game errors. Correct trials produced lower correlation between the medial frontal gyrus and other ROIs during both self-committed and observed game errors. Matrices including pairwise correlation coefficients between error-related BOLD responses in the 23 ROIs are presented in Fig. 12.

Coordinates				p**-values**		
	x	**y**	**z**	**game vs. nat**	**obs vs. nat**	**game vs. obs**
Dorsal ACC L	-8	20	30	0.00430	0.05126	0.00000
Dorsal ACC R	6	20	30	0.00107	0.05135	0.00000
Inferior frontal gyrus L	-44	16	2	0.00157	0.73573	0.00042
Inferior frontal gyrus R	46	14	8	0.00319	0.03900	0.16755
Insula L	-44	10	-4	0.06679	0.24315	0.00308
Insula R	32	26	0	0.00039	0.52674	0.00036
Medial frontal gyrus	0	48	24	0.00250	0.00403	0.99010
Middle temporal gyrus L	-54	2	-20	0.05150	0.00736	0.46777
Middle temporal gyrus R	52	8	-32	0.00476	0.00003	0.23043
Supramarginal gyrus L	-66	-28	20	0.00601	0.31590	0.06065
Supramarginal gyrus R	60	-40	18	0.04864	0.83610	0.05333
Superior frontal gyrus R	6	14	56	0.00019	0.27011	0.00104
Superior frontal gyrus L	-6	16	56	0.00060	0.27918	0.00451
Putamen L	-18	8	-8	0.08712	0.01999	0.00017
Putamen R	18	10	-8	0.01517	0.03626	0.00004
Pallidum L	-22	-8	0	0.42397	0.14732	0.01042
Pallidum R	20	-4	0	0.08515	0.08391	0.00028
Caudate L	-14	12	12	0.73298	0.47484	0.60795
Caudate R	16	20	4	0.53613	0.30931	0.04456
Visual Cortex L	-12	-74	-12	0.93752	0.00179	0.00086
Visual Cortex R	12	-74	-12	0.66873	0.00008	0.00122
Rostral ACC L	-2	34	2	0.08409	0.01063	0.14451
Rostral ACC R	2	34	2	0.08722	0.00591	0.07477

Table 1: MNI coordinates of ROIs and the significance values for peak activation differences between conditions.

Also the percent signal change at 4 s in several ROIs differed significantly between conditions. During self-committed errors, activation in the dACC, superior frontal gyrus, right insula, left inferior frontal gyrus and right putamen was significantly higher than during either of the observed errors. Naturalistic errors caused significantly higher activity in the medial frontal gyrus and right middle temporal gyrus compared to the other conditions. Observed game errors did not cause significantly higher activity in any of the ROIs compared to the other two conditions. The

coordinates for ROIs (MNI space) and the p-values reflecting the significance of the between-condition difference are presented in table 1. Mean percent signal changes, standard errors of the mean (SEM) and significance levels of the between-condition differences are presented in Fig. 13.

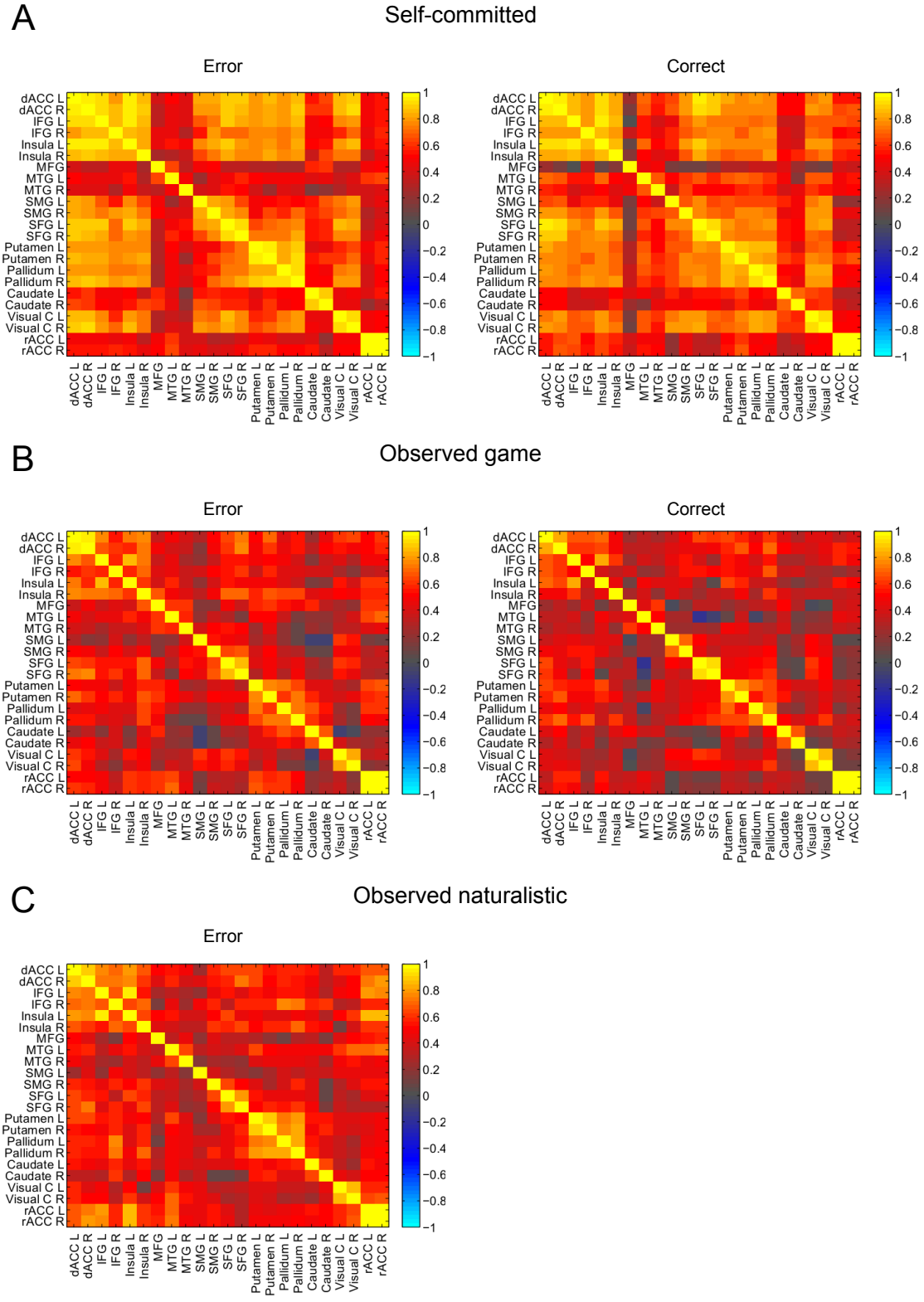

Figure 12: Correlations between error-related BOLD responses in 23 ROIs in during A) self-committed errors, B) observed game errors, C) naturalistic errors.

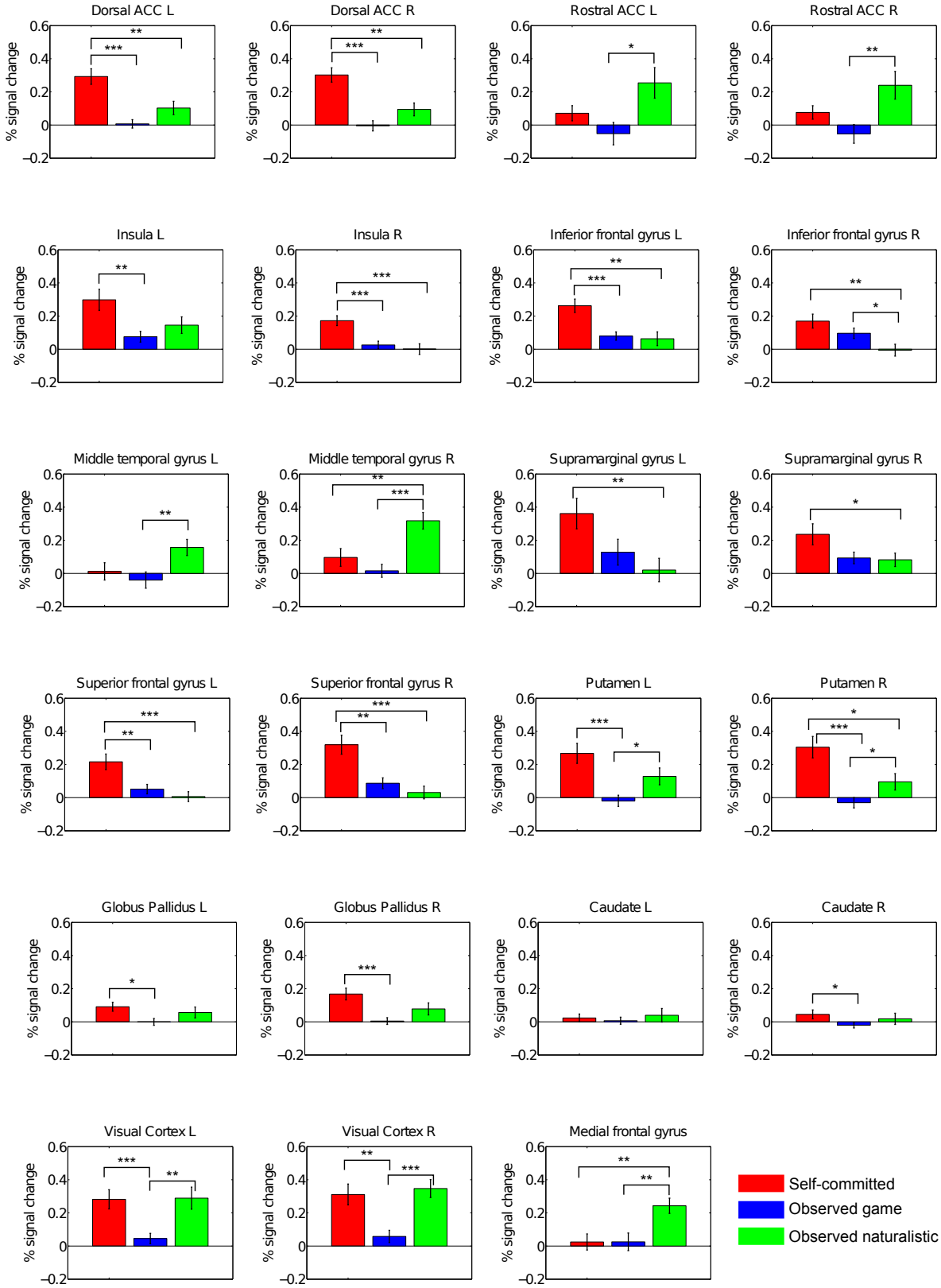

Figure 13: Error-related % signal change +/- SEM 4 s after errors in 23 ROIs in different error conditions. Stars above bars indicate the significance of the difference. *=p<0.05, **=p<0.01, ***=p<0.001.

6.4 ICA

The results of ICA reflected the results of the GLM analyses. Error-related components, indicated by significant contrasts of beta weights, were detected in self-committed and naturalistic error conditions. In the observed game condition, none of the components was more modulated by errors than correct trials. However, IC04, including mostly visual cortical areas (occipital pole, lingual gyrus, occipital fusiform gyrus), was significantly modulated by both errors ($p<0.001$, $t=6.826$) and correct trials ($p<0.001$, $t=6.730$).

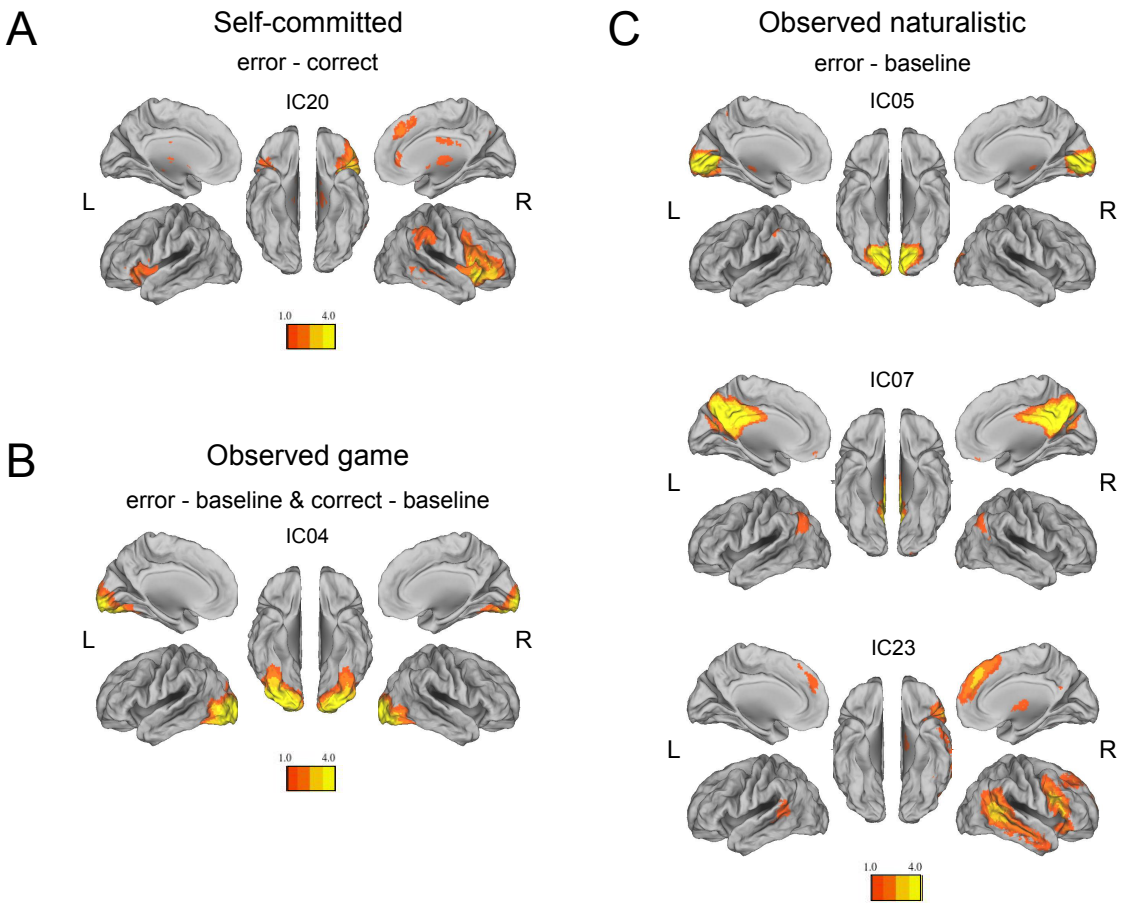

Figure 14: Z-statistical maps of independent components significantly related to A) self-committed errors, B) both errors and correct trials in the observed game, C) naturalistic errors. The colors represent the contribution of each voxel to the IC time course.

One component was significantly related to the self-committed errors. IC20 ($F_{1,17}=4.555$, $p=0.040$) included the dACC, frontal pole, bilateral inferior frontal gyrus, left thalamus and orbitofrontal cortex.

Naturalistic observed errors were significantly associated with three distinct components. IC05 ($F_{1,17}=47.262$, $p<0.001$) included visual cortical regions (lingual

gyrus, occipital fusiform gyrus), IC07 ($F_{1,17}$=14.704, p<0.001) included the lateral occipital cortex, cuneus and PCC, and IC23 ($F_{1,17}$=39.779, p<0.001) included prefrontal regions (frontal pole, superior and middle frontal gyri), middle temporal gyrus, posterior superior temporal gyrus and paracingulate gyrus.

Spatial maps of all error-related ICs are presented in Fig. 14. As the focus of this study was strictly on the neural circuits subserving error processing, we did not analyze the ICs unrelated to errors, e.g. the default mode network or somatosensory networks.

6.4.1 Comparison between GLM and ICA results

The activation patterns found by GLM and ICA were similar, but not identical. Neither GLM nor ICA revealed significant error-specific activation in the observed game condition, and naturally the activation maps from the two approaches do not overlap in this condition. In the self-committed and naturalistic conditions, the IC maps included mostly the same regions as the statistical parametric maps obtained by GLM.

However, the IC maps contained also additional regions that were not found by GLM, and vice versa. For example, in the self-committed condition IC20 included the rACC, although in the GLM map showed significant activation only in the dACC. Also, the IC map was more extensive in the right inferior frontal cortex. In contrast, IC20 did not include activation in the dACC or SMA. In the naturalistic condition the three error-related components largely overlap with the regions shown the GLM map. However, the spatial maps of IC07, containing the cuneus and precuneus, and IC23, containing the medial and inferior frontal cortices, were clearly more extensive than the GLM activation in these regions.

The GLM activation maps, overlaid on IC spatial maps for the corresponding task conditions, are presented in Fig. 15.

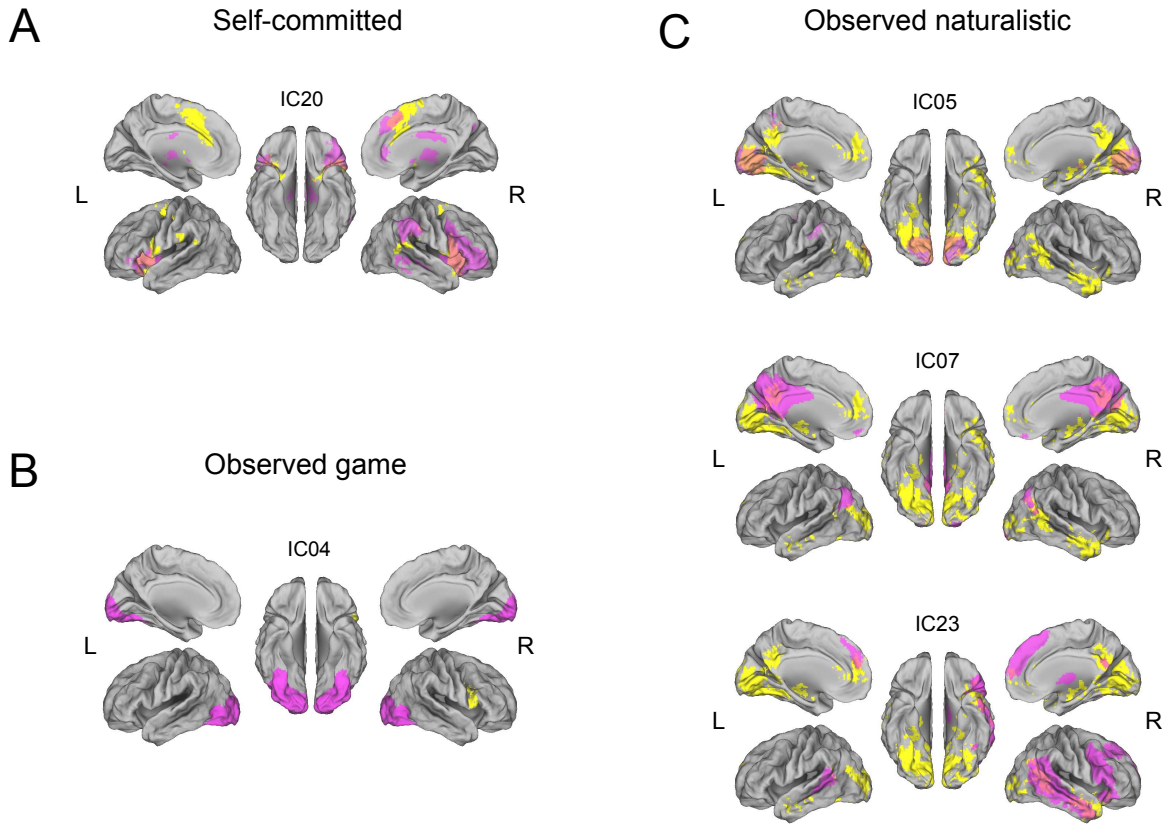

Figure 15: ICA spatial maps (purple) overlaid on maximal GLM activation maps (yellow) corresponding to A) the self-committed condition, B) the observed game condition, C) the naturalistic condition. The colors are arbitrary and represent only the spatial extent of the maps.

7 Discussion

In this study, we examined the neural correlates of self-committed and observed errors with fMRI. The aim was to investigate whether the human brain processes errors differently depending on the viewpoint, i.e. whether errors committed by oneself and others produce different activation patterns. Using subjective ratings for error intensity and anticipation, both the likelihood of errors and the degree of incorrectness in the naturalistic video clips were evaluated and used as modulators of the GLM regressors. In addition, analyses of functional connectivity were performed with ROI-based correlation measures and data-driven independent component analysis.

7.1 Error-related BOLD responses in different conditions

The GLM analyses revealed robust error-related hemodynamic activity in self-committed and naturalistic conditions, but not in the observed game condition. Error-related activity during self-committed errors was significant in regions usually implicated in error monitoring, i.e. dACC, inferior frontal gyrus, insula and putamen. Activity in the dACC was expected, as the region is previously found to encode on-line performance evaluation [Shackman et al., 2011; Taylor et al., 2006; van Veen and Carter, 2002]. Activation of bilateral insula was especially interesting, as it is assumed that simultaneuous activity of ACC and insula modulates awareness and motivation [Medford and Critchley, 2010]. It is likely that errors in the video game enhanced the subjects' focus on the game, which was reflected in their brain activity.

Perhaps even more intriguing was the activation pattern of the striatum: error trials produced increased activity in the bilateral putamen at 4 s when compared with correct trials, but the correct trials elicited increased activity in the whole striatum at 6 s. As the striatum is responsible for processing reward and punishment [Delgado, 2007], it is not surprising that striatal activation was produced by both emotionally positive correct trials and negative error trials. The resulting contrast images can be interpreted such that the BOLD activation peaked strongly after errors and then gradually decreased, whereas after correct trials both the peak and the decrease of the response were lower. These different responses resulted in slightly higher error-specific activity at 4 s and higher correct-specific activity at 6 s. A highly consistent finding was done by Delgado et al. [2000]. In their study the striatal BOLD activity peaked rapidly and then decreased after punishment, but remained nearly constant after reward, resulting in a higher BOLD signal 6 s after correct trials. Furthermore, in our study the self-committed errors caused increased activity in the midbrain, specifically in the red nucleus and substantia nigra. This finding agrees with the suggestion that activation of the midbrain dopamine system is a main modulator of ACC activation and a generator of the ERN [Holroyd and Coles, 2002].

Observed game errors failed to produce robust BOLD responses in ACC and other regions implicated in performance monitoring. A plausible explanation for this finding is that the task was simply not engaging enough to elicit significant

activity. Even though the contrast between errors and correct trials showed activity in the inferior frontal gyri and bilateral middle temporal cortices at 2 s, it was considered noise because of the short latency. It is unlikely that the peak of BOLD response would occur at 2 s even though the stimulus was very short. However, it is not extremely surprising that this kind of task did not produce error-related activity in the ACC or striatum, as in a simple task it is quite difficult to learn from the mistakes of others, let alone empathize with the invisible player. Considering these aspects, it is justified to use naturalistic stimulus paradigms in further studies of processing observed errors.

The activation caused by naturalistic errors was especially prominent in visual cortical areas (lingual gyrus) and cerebellum. Similar activity was detected in these regions during self-committed errors. According to Danielmeier et al. [2011], errors might enhance activity in perceptual areas encoding task-relevant stimulus features, which would explain the increased hemodynamic activity in visual regions after errors. Another significantly activated region during naturalistic errors was the anterior medial frontal gyrus, which was located close to the rACC. Our hypothesis about enhanced emotional valence related to observed naturalistic errors is supported by this finding, since rACC is frequently implicated in affective processing of errors [Bush et al., 2000; Manoach and Agam, 2013]. It seems that watching people failing in everyday situations produced empathetic responses, as expected. When the effect of pain was regressed out of the data, the activity in rACC and medial prefrontal cortex was diminished, indicating that watching someone feeling pain was enhancing the emotional responses. Pain intensity is known to increase the affective responses in ACC [Jackson et al., 2005; Lloyd et al., 2004]. However, the previous studies localized pain responses to the dACC, whereas our findings suggested increased activity in the rACC.

7.2 Differences between conditions

There were several remarkable differences in the activation of peak ROIs between error conditions. Dorsal ACC was significantly ($p<0.001$) more activated during self-committed errors than during observed game or naturalistic errors. This gives further evidence about the role of this region in on-line performance monitoring. Errors in the active playing task probably signaled an immediate need for behavioral adjustments, which were not required after observed errors. Thus, it is logical that the region mediating performance monitoring activated only in the game playing condition. However, rostral ACC activation did not show any difference between self-committed and naturalistic errors, although it differed significantly between observed game and naturalistic conditions. In light of this finding, it can be hypothesized that the affective component of errors is quite similar when the subjects fail themselves and watch other people fail, but almost nonexistent when they are watching simulated, non-naturalistic game errors where human beings are not visible.

The contrast between self-committed and observed naturalistic error responses revealed increased activity in the bilateral insula and medial frontal gyrus during self-

committed errors and increased activity in the posterior cingulate, superior frontal gyrus and superior temporal gyrus during naturalistic errors. Also the comparison between error-related percent signal changes revealed significant differences between self-committed and naturalistic errors in the right insula ($p<0.001$). Also, activation of the right putamen was significantly ($p<0.05$) stronger during self-commmitted errors, but other striatal subregions did not show significant differences between conditions. As a conclusion, the striatal activity was quite similar, but not identical, during self-committed and observed naturalistic errors. Regarding this result, it can be hypothesized that similar reward and punishment signals might be elicited during both conditions, but the striatal activity is more robust after self-committed errors. Perhaps the timing of naturalistic errors was not specific enough to distinguish accurate BOLD responses; in the self-committed condition the response was always clearly time-locked to the error, but that was not necessarily the case for naturalistic errors. The latency of the striatal response might have differed between subjects, depending on their subjective experience about the reward value of observed errors.

7.3 Effect of error anticipation

The contrasts between error anticipation and observation in the naturalistic condition yielded interesting results. Several regions associated with performance monitoring, including insula, striatum, dorsal ACC and primary somatosensory cortex (postcentral gyrus), were activated already during error anticipation. However, visual cortical regions and rostral ACC showed increased activation after errors compared to error anticipation. When anticipated and surprising errors were contrasted with each other, quite similar distinction was detected: anticipated errors activated mainly the visual cortical areas, whereas surprising errors elicited activation in the anterior dACC. This result agrees to a great extent with the findings done by Schiffer et al. [2013]; they showed that unexpectedness of errors is the main factor contributing to the activation of the rostral cingulate zone, which highly corresponds to the location of activity in our study.

In addition, the current results suggest differential roles for rostral and dorsal ACC in error monitoring: the former showed increased activation during error occurrence and surprising errors in the naturalistic condition, and the latter during error anticipation and self-committed errors. We can speculate that dACC responds specifically to the increased likelihood of errors, as the probability of erroneous action was maximal during self-generated errors and increased during anticipation of errors. Thus, dACC might indeed encode the increased need for cognitive control in the presence of high error likelihood, as proposed by Brown and Braver [2005]. In contrast, rACC seems to signal the affective significance of errors: it was activated similarly during commitment of errors and observation of naturalistic errors and showed increased activity due to painful observed errors, which probably elicit strong emotions. The distinction between dACC and rACC has been observed in neuroanatomical studies, e.g. by [Palomero-Gallagher et al., 2009], and the differential contributions of these regions to error monitoring was validated in an fMRI study [Polli et al., 2005]. Our findings support the previous theories and shed fur-

ther light on the distinct components of the error processing circuit. The results are also consistent with the 'action-outcome predictor' model introduced by Alexander and Brown [2011], as dACC responded both to the anticipation of errors and the occurrence of unexpected self-generated errors.

7.4 Functional connectivity during error monitoring

Error-related functional connectivity was investigated using both ICA and ROI-based correlation analyses. The results are not directly comparable due to methodological differences, but the inferences drawn from both analyses support the findings from the GLM analysis.

The correlations between BOLD responses were high within a network containing dACC, insula, prefrontal cortex and striatum during self-committed errors. The connectivity between striatal subregions and dACC/inferior frontal gyrus was also very high during naturalistic errors, but the correlations between the striatum and the dACC/mPFC network were quite low. The connectivity between all ROIs was the weakest during observed game errors, implying a generally less coordinated brain activity in that condition. Furthermore, the correlations between striatal subregions were lower during observed successful trials than self-committed successful trials. This result can be interpreted such that the observed game was not capable of eliciting reward sensations mediated by the striatum, whereas self-made correct trials elicited instant feelings of reward.

The results obtained by ICA reflected another perspective about error-related brain function. The finding that similar regions appeared in both the GLM activations and the most error-related ICs indicates that the significantly error-related brain regions were also functionally connected during error processing. Thus, the ICA results imply that these regions are parts of a synchronized error-monitoring network, rather than isolated regions functioning independently of each other. Further support for this finding was given by the high correlations between the most activated ROIs in each condition.

Self-committed errors showed significant associations with a single component consisting of the rACC, paracingulate gyrus, bilateral inferior frontal cortex, supramarginal gyrus and thalamus, implying the contribution of these regions to the error monitoring circuit. The result is consistent with the finding that these regions also showed high correlations between each other in the ROI analysis.

Interestingly, the naturalistic observed errors were associated with three distinct ICs, which together covered the activated regions found by GLM. This finding suggests that processing of observed errors recruits multiple spatially separate neural circuits. IC05 included the visual cortex, IC07 the cuneus and precuneus, and IC23 the paracingulate gyrus, inferior frontal gyrus, bilateral middle temporal gyrus and thalamus. We can thus suggest that these networks are functioning simultaneously, but independently of each other, probably encoding different stimulus aspects. Reducing the predefined data dimensionality would perhaps result in larger components and group these segregated networks together. However, the dimensionality was fairly small (25 components), implying that the statistical independence between

the resulting components was already high.

In the observed game condition, none of the ICs showed error-specific modulations of activity. Instead, a component in the visual cortex showed significant activation in response to both errors and correct trials, possibly reflecting an enhanced focus on visual stimuli due to the visual feedback after each trial. The absence of error-related components is consistent with the GLM results, which did not indicate significant differences in ACC or other error monitoring regions between responses to errors and correct trials in the observed game condition.

In all experimental conditions, ICA found several regions not detected by the GLM analysis. The explanation for this arises from the nature of ICA: all voxels belonging to the same component do not necessarily have identical activation time courses, but they are not different enough to be statistically independent. In GLM the regressor model is fitted to the time courses of each voxel separately, so even the slightly deviating voxels may not exceed the significance level. In ICA the regressor model is fitted to the average time course of each component, i.e. the significance levels are calculated for the whole component regardless of the contribution of individual voxels. On the other hand, voxel time courses used in GLM may have a low SNR, which causes bias in the results if not included in the design matrix. ICA is able to separate the noise components from the meaningful signals and may thus detect even minor underlying activations.

According to these findings, ICA can detect similar activation patterns as GLM and probably even expand the GLM results, if conducted with appropriate parameters and data dimensionality. A great benefit of ICA is the ability to provide information about event-related functional connectivity. Also, IC time courses generally have a higher SNR than voxel time courses. Therefore, ICA can detect minor event-related signal changes better than GLM as long as the requirement of statistical independence between signal and noise components is fulfilled. However, it should be emphasized that the optimal number of components is still rather difficult to determine. In this study the automated MDL algorithm failed to produce stable component estimates and the dimensionality had to be reduced manually. However, regarding that the components obtained with the reduced dimensionalities were very stable over multiple ICASSO runs, it is likely that they reflect the actual independent signal sources. As a conclusion, methods for group-level ICA and dimensionality estimation should be improved in order to accomplish more reliable results from event-related fMRI studies.

7.5 Limitations

The current study included certain limitations, which might affect the statistical significance of the results. The most prominent limitation was the inhomogeneity of the subject groups in different experimental conditions. Several subjects made excessive head motion during some of the three tasks, but it was not desirable to discard all runs of the subject because of one unusable run. Instead, each task was processed separately, including only the motion-free subjects. However, this procedure was problematic only when comparing the activations in different task

conditions. Especially, the significance levels in the between-condition comparison of error responses were somewhat biased, because they were defined by a two-sample t-test instead of a paired t-test.

The fact that the subjects made different numbers of errors could also be criticized when evaluating the significance of activity produced by self-committed errors. Some subjects made almost the same number of errors and correct trials. In this case the unexpectedness of errors was practically absent, as it was equally probable to commit an error and a correct response. However, most subjects performed reasonably well and made less errors than correct trials, so this confound was not likely to affect the group-level results. In the following studies the stimulus paradigm could be modified by adjusting the game speed according to the error rate; this approach is commonly used in so-called speeded response selection tasks.

Another considerable limitation arised from the number of errors in the naturalistic task. The video clips included in total 35 errors, but only about 20 of them were rated as relevant (rating >0.5) by the subjects. Out of these 20 errors, 10 were considered surprising and 10 anticipated, according to the values of anticipation ratings preceding each error rating. This number is rather low, considering that the aim was to average error-related responses and make contrasts between anticipated and surprising errors. The small sample size increases the risk for type II errors, i.e. not detecting the existing responses. Therefore, increasing the number of errors might enhance the detection accuracy in similar studies.

7.6 Applications for further research

This study provided new information about the neural mechanisms of error processing in healthy individuals. As the errors in naturalistic video clips elicited significant brain activity in this subject group, we could consider the possibility of extending this study into clinical patients. It would be intriguing to study the error responses of e.g. Parkinson's disease patients having deficits in the midbrain dopamine system, as these deficits might affect processing of both self-committed and observed errors. On the other hand, more complex psychiatric disorders, such as schizophrenia and OCD, would be worth investigating in terms of observed error processing, since it is already known that both diseases cause abnormal responses to self-committed errors [Fitzgerald et al., 2005; Sanders et al., 2002].

Considering the high accuracy required in clinical studies, we could improve the analysis methods by using combined fMRI-EEG. The great advantage of this multimodal imaging method is the possibility to construct the fMRI regressors based on the ERP peaks. When conducting an fMRI analysis, it has to be assumed that all errors produce a similar BOLD response. However, some errors might be left unnoticed by the subject, thus not producing a response; this factor is especially noteworthy when studying patients with attention deficits. As a result, the predefined regressors will be biased, which may lead to spurious results. The EEG signal could be used to predict the waveforms of the BOLD signal (and probably vice versa) in the multimodal approach, which could improve the accuracy of detecting error responses. The majority of error processing research is ERN studies based on

EEG, and a great amount of fMRI measurements have confirmed the ERN findings. The EEG-fMRI analysis would give a sound proof about the relationship between the ERN and the error-related BOLD activity. The conjoint analysis could also refine our findings about the activation related to error anticipation. Thus, it would be worth studying, even though the multimodal method requires a rather difficult set-up and more signal processing.

It could also be useful to apply multimodal ICA [Eichele et al., 2008; Moeller et al., 2011] to EEG-fMRI for spatio–temporal segregation of event-related activation patterns. The results from the current study showed that ICA is able to detect event-related activations in fMRI data, so it would be interesting to apply it in the multimodal approach. Multimodal ICA has already been used in a performance monitoring task by [Huster et al., 2011]. By using a cross-modal correlation between the ICs from EEG and fMRI data, they were able to accurately distinguish multiple task-related networks.

Another possibility for the future is to bring the naturalistic scenario even further and utilize multi-subject scanning methods (see a review by Konvalinka and Roepstorff [2012]) in the observation condition. For example, two persons in separate MRI scanners or MEG shielded rooms could play a simple game and communicate in real time via a video call. The subjects could play the game in turns and observe each other's mistakes, either expected or unexpected. The most novel possibility for multi-subject experiments is two-person fMRI, in which both subjects are lying face-to-face in the same scanner and being scanned simultaneously. In a two-person set-up, it would be possible to design a task involving some kind of social interaction. The observed errors could be e.g. inappropriate responses or breaking of social norms and expectations. Since this study showed that striatal activity was evoked by error observation during the naturalistic scenario, it would very likely that erroneous or unexpected responses in real time social interaction would activate the striatum as well. This kind of interactive task would also propose an effective method for studying inter-subject correlation during error monitoring, which would yield new insights about the neural mechanisms related to social behavior.

8 Conclusions

The results of the current study suggested that similar neural mechanisms are recruited during processing of errors committed by oneself and others. Activation of the striatum and rostral ACC during both self-committed and observed naturalistic errors constitutes a hypothesis that the affective significance of errors is similar in these situations. Furthermore, increased activity of the dorsal ACC, insula and inferior frontal gyrus during self-committed errors and anticipation of observed naturalistic errors suggests that these regions encode the likelihood of errors and a need for behavioral adjustments. The absence of an error-related BOLD response during the observed game condition implies that naturalistic paradigms are more effective in eliciting empathetic responses to errors made by others, and should therefore be used instead of controlled stimulus paradigms.

The GLM approach was efficient in revealing error-related BOLD responses. With the FIR model it was easy to extract responses of any shape and detect the moment of peak error-related activation. Furthermore, implementing multiple contrasts between explanatory variables and experimental conditions was straightforward with the GLM model. ICA could also be used to detect similar error-related networks, but the difficulty to determine the optimal data dimensionality decreased the reliability of ICA in this study. ROI-based correlation analysis could be used as a good complementary method for investigating functional connectivity during error monitoring, especially when the regions of peak activation were used as ROIs. To conclude, GLM is a good analysis method for event-related fMRI studies, especially if conducted with flexible convolution models.

References

Alexander, W. H. and Brown, J. W. (2011). Medial prefrontal cortex as an action-outcome predictor. *Nature neuroscience*, 14(10):1338–1344.

Bandettini, P. A. and Cox, R. W. (2000). Event-related fmri contrast when using constant interstimulus interval: Theory and experiment. *Magnetic Resonance in Medicine*, 43(4):540–548.

Bell, A. J. and Sejnowski, T. J. (1995). An information-maximization approach to blind separation and blind deconvolution. *Neural computation*, 7(6):1129–1159.

Beste, C., Saft, C., Andrich, J., Gold, R., and Falkenstein, M. (2006). Error processing in huntington's disease. *PLoS One*, 1(1):e86.

Botvinick, M. M., Braver, T. S., Barch, D. M., Carter, C. S., and Cohen, J. D. (2001). Conflict monitoring and cognitive control. *Psychological review*, 108(3):624.

Braver, T. S., Barch, D. M., Gray, J. R., Molfese, D. L., and Snyder, A. (2001). Anterior cingulate cortex and response conflict: effects of frequency, inhibition and errors. *Cerebral Cortex*, 11(9):825–836.

Brown, J. W. and Braver, T. S. (2005). Learned predictions of error likelihood in the anterior cingulate cortex. *Science*, 307(5712):1118–1121.

Bush, G., Luu, P., and Posner, M. I. (2000). Cognitive and emotional influences in anterior cingulate cortex. *Trends in cognitive sciences*, 4(6):215–222.

Calhoun, V., Adali, T., Pearlson, G., and Pekar, J. (2001). A method for making group inferences from functional mri data using independent component analysis. *Human brain mapping*, 14(3):140–151.

Carter, C. S. (1998). Anterior Cingulate Cortex, Error Detection, and the Online Monitoring of Performance. *Science*, 280(5364):747–749.

Carter, C. S., Mintun, M., Nichols, T., and Cohen, J. D. (1997). Anterior cingulate gyrus dysfunction and selective attention deficits in schizophrenia:[15o] h2o pet study during single-trial stroop task performance. *American Journal of Psychiatry*, 154(12):1670–1675.

Chavhan, G. B., Babyn, P. S., Thomas, B., Shroff, M. M., and Haacke, E. M. (2009). Principles, techniques, and applications of t2*-based mr imaging and its special applications. *Radiographics*, 29(5):1433–1449.

Corey, D. M., Dunlap, W. P., and Burke, M. J. (1998). Averaging correlations: Expected values and bias in combined pearson rs and fisher's z transformations. *The Journal of general psychology*, 125(3):245–261.

Dale, A. M. and Buckner, R. L. (1997). Selective averaging of rapidly presented individual trials using fmri. *Human brain mapping*, 5(5):329–340.

Danielmeier, C., Eichele, T., Forstmann, B. U., Tittgemeyer, M., and Ullsperger, M. (2011). Posterior medial frontal cortex activity predicts post-error adaptations in task-related visual and motor areas. *The Journal of Neuroscience*, 31(5):1780–1789.

de Bruijn, E. R., de Lange, F. P., von Cramon, D. Y., and Ullsperger, M. (2009). When errors are rewarding. *The Journal of Neuroscience*, 29(39):12183–12186.

Delgado, M. R. (2007). Reward-related responses in the human striatum. *Annals of the New York Academy of Sciences*, 1104(1):70–88.

Delgado, M. R., Nystrom, L. E., Fissell, C., Noll, D., and Fiez, J. A. (2000). Tracking the hemodynamic responses to reward and punishment in the striatum. *Journal of neurophysiology*, 84(6):3072–3077.

Egner, T., Delano, M., and Hirsch, J. (2007). Separate conflict-specific cognitive control mechanisms in the human brain. *Neuroimage*, 35(2):940–948.

Eichele, T., Calhoun, V. D., Moosmann, M., Specht, K., Jongsma, M. L., Quiroga, R. Q., Nordby, H., and Hugdahl, K. (2008). Unmixing concurrent eeg-fmri with parallel independent component analysis. *International Journal of Psychophysiology*, 67(3):222–234.

Evans, A., Collins, D., and Milner, B. (1992). An mri-based stereotactic atlas from 250 young normal subjects. In *Soc. neurosci. abstr*, volume 18, page 408.

Falkenstein, M., Hielscher, H., Dziobek, I., Schwarzenau, P., Hoormann, J., Sundermann, B., and Hohnsbein, J. (2001). Action monitoring, error detection, and the basal ganglia: an erp study. *Neuroreport*, 12(1):157–161.

Fitzgerald, K. D., Welsh, R. C., Gehring, W. J., Abelson, J. L., Himle, J. a., Liberzon, I., and Taylor, S. F. (2005). Error-related hyperactivity of the anterior cingulate cortex in obsessive-compulsive disorder. *Biological psychiatry*, 57(3):287–94.

Friston, K. J., Holmes, A. P., Worsley, K. J., Poline, J.-P., Frith, C. D., and Frackowiak, R. S. (1994). Statistical parametric maps in functional imaging: a general linear approach. *Human brain mapping*, 2(4):189–210.

Garavan, H., Ross, T., Murphy, K., Roche, R., and Stein, E. (2002). Dissociable executive functions in the dynamic control of behavior: inhibition, error detection, and correction. *Neuroimage*, 17(4):1820–1829.

Gehring, W. J., Goss, B., Coles, M. G. H., Meyer, D. E., and Donchin, E. (1993). A neural system for error detection and compensation. *Psychological Science*, 4(6):385–390.

Gotlib, I. H., Sivers, H., Gabrieli, J. D. E., Whit, S., Goldin, P., and Minor, K. L. (2005). Subgenual anterior cingulate activation to valenced emotional stimuli in major depression. *Neuroreport*, 16(16).

Henson, R., Rugg, M. D., and Friston, K. J. (2001). The choice of basis functions in event-related fmri. *Neuroimage*, 13(6):149–149.

Hohnsbein, J., Falkenstein, M., and Hoorman, J. (1989). Error processing in visual and auditory choice reaction tasks. *Journal of Psychophysiology*, 3:32.

Holroyd, C. B. and Coles, M. G. (2002). The neural basis of human error processing: reinforcement learning, dopamine, and the error-related negativity. *Psychological review*, 109(4):679.

Huettel, S. A., Song, Allen W., ., and McCarthy, Gregory, . (2004). *Functional magnetic resonance imaging / Scott A. Huettel, Allen W. Song, Gregory McCarthy.* Sunderland, Mass. : Sinauer Associates ; Basingstoke : Palgrave, 1st ed edition.

Huster, R. J., Eichele, T., Enriquez-Geppert, S., Wollbrink, A., Kugel, H., Konrad, C., and Pantev, C. (2011). Multimodal imaging of functional networks and event-related potentials in performance monitoring. *Neuroimage*, 56(3):1588–1597.

Hyvärinen, A. and Oja, E. (2000). Independent component analysis: algorithms and applications. *Neural networks : the official journal of the International Neural Network Society*, 13(4-5):411–30.

Ito, J. and Kitagawa, J. (2006). Performance monitoring and error processing during a lexical decision task in patients with parkinson's disease. *Journal of geriatric psychiatry and neurology*, 19(1):46–54.

Jackson, P. L., Meltzoff, A. N., and Decety, J. (2005). How do we perceive the pain of others? a window into the neural processes involved in empathy. *Neuroimage*, 24(3):771–779.

Jenkinson, M., Bannister, P., Brady, M., and Smith, S. (2002). Improved optimization for the robust and accurate linear registration and motion correction of brain images. *Neuroimage*, 17(2):825–841.

Kätsyri, J., Hari, R., Ravaja, N., and Nummenmaa, L. (2013). Just watching the game ain't enough: Striatal fmri reward responses to successes and failures in a video game during active and vicarious playing. *Frontiers in Human Neuroscience*, 7(278).

Kiehl, K. A., Liddle, P. F., and Hopfinger, J. B. (2000). Error processing and the rostral anterior cingulate: An event-related fmri study. *Psychophysiology*, 37(2):216–223.

Kim, D. I., Mathalon, D., Ford, J., Mannell, M., Turner, J., Brown, G., Belger, A., Gollub, R., Lauriello, J., Wible, C., et al. (2009). Auditory oddball deficits in schizophrenia: an independent component analysis of the fmri multisite function birn study. *Schizophrenia bulletin*, 35(1):67–81.

Konvalinka, I. and Roepstorff, A. (2012). The two-brain approach: how can mutually interacting brains teach us something about social interaction? *Frontiers in human neuroscience*, 6.

Kopp, B. and Rist, F. (1999). An event-related brain potential substrate of disturbed response monitoring in paranoid schizophrenic patients. *Journal of abnormal psychology*, 108(2):337.

Kwong, K. K., Belliveau, J. W., Chesler, D. A., Goldberg, I. E., Weisskoff, R. M., Poncelet, B. P., Kennedy, D. N., Hoppel, B. E., Cohen, M. S., and Turner, R. (1992). Dynamic magnetic resonance imaging of human brain activity during primary sensory stimulation. *Proceedings of the National Academy of Sciences*, 89(12):5675–5679.

Lahnakoski, J. (2010). Functional magnetic resonance imaging of human brain during rest and viewing movies. *Master's Thesis, Faculty of Electronics, Communications and Automation, Aalto University School of Science and Technology.*

Laurens, K. R. (2003). Rostral anterior cingulate cortex dysfunction during error processing in schizophrenia. *Brain*, 126(3):610–622.

Ljunggren, S. (1983). A simple graphical representation of fourier-based imaging methods. *Journal of Magnetic Resonance (1969)*, 54(2):338–343.

Lloyd, D., Di Pellegrino, G., and Roberts, N. (2004). Vicarious responses to pain in anterior cingulate cortex: is empathy a multisensory issue? *Cognitive, Affective, & Behavioral Neuroscience*, 4(2):270–278.

Malinen, S., Hlushchuk, Y., and Hari, R. (2007). Towards natural stimulation in fMRI–issues of data analysis. *NeuroImage*, 35(1):131–9.

Manoach, D. S. and Agam, Y. (2013). Neural markers of errors as endophenotypes in neuropsychiatric disorders. *Frontiers in Human Neuroscience*, 7(350).

Mansfield, P. (1977). Multi-planar image formation using nmr spin echoes. *Journal of Physics C: Solid State Physics*, 10(3):L55.

Mathalon, D. H., Fedor, M., Faustman, W. O., Gray, M., Askari, N., and Ford, J. M. (2002). Response-monitoring dysfunction in schizophrenia: An event-related brain potential study. *Journal of Abnormal Psychology*, 111(1):22–41.

Medford, N. and Critchley, H. D. (2010). Conjoint activity of anterior insular and anterior cingulate cortex: awareness and response. *Brain Structure and Function*, 214(5-6):535–549.

Menon, V., Adleman, N. E., White, C., Glover, G., and Reiss, A. (2001). Error-related brain activation during a go/nogo response inhibition task. *Human Brain Mapping*, 12(3):131–143.

Miltner, W. H., Brauer, J., Hecht, H., Trippe, R., and Coles, M. G. (2004). Parallel brain activity for self-generated and observed errors. *Errors, conflicts, and the brain: Current opinions on performance monitoring*, pages 124–129.

Moeller, F., LeVan, P., and Gotman, J. (2011). Independent component analysis (ica) of generalized spike wave discharges in fmri: Comparison with general linear model-based eeg-fmri. *Human brain mapping*, 32(2):209–217.

Ogawa, S., Lee, T., Kay, A., and Tank, D. (1990). Brain magnetic resonance imaging with contrast dependent on blood oxygenation. *Proceedings of the National Academy of Sciences*, 87(24):9868–9872.

Palomero-Gallagher, N., Vogt, B. A., Schleicher, A., Mayberg, H. S., and Zilles, K. (2009). Receptor architecture of human cingulate cortex: Evaluation of the four-region neurobiological model. *Human brain mapping*, 30(8):2336–2355.

Paus, T. (2001). Primate anterior cingulate cortex: where motor control, drive and cognition interface. *Nature Reviews Neuroscience*, 2(6):417–424.

Polli, F. E., Barton, J. J., Cain, M. S., Thakkar, K. N., Rauch, S. L., and Manoach, D. S. (2005). Rostral and dorsal anterior cingulate cortex make dissociable contributions during antisaccade error commission. *Proceedings of the National Academy of Sciences of the United States of America*, 102(43):15700–15705.

Polli, F. E., Barton, J. J., Thakkar, K. N., Greve, D. N., Goff, D. C., Rauch, S. L., and Manoach, D. S. (2008). Reduced error-related activation in two anterior cingulate circuits is related to impaired performance in schizophrenia. *Brain*, 131(4):971–986.

Poustchi-Amin, M., Mirowitz, S., Brown, J., McKinstry, R., and Li, T. (2001). Principles and Applications of Echo-planar Imaging : A Review for the General Radiologist. *Radiographics*, pages 767–779.

Rorden, C., Karnath, H.-O., and Bonilha, L. (2007). Improving lesion-symptom mapping. *Journal of cognitive neuroscience*, 19(7):1081–1088.

Sanders, G. S., Gallup Jr, G. G., Heinsen, H., Hof, P. R., and Schmitz, C. (2002). Cognitive deficits, schizophrenia, and the anterior cingulate cortex. *Trends in cognitive sciences*, 6(5):190–192.

Schiffer, A.-M., Krause, K. H., and Schubotz, R. I. (2013). Surprisingly correct: Unexpectedness of observed actions activates the medial prefrontal cortex. *Human brain mapping*.

Shackman, A. J., Salomons, T. V., Slagter, H. A., Fox, A. S., Winter, J. J., and Davidson, R. J. (2011). The integration of negative affect, pain and cognitive control in the cingulate cortex. *Nature Reviews Neuroscience*, 12(3):154–167.

Shane, M. S., Stevens, M., Harenski, C. L., and Kiehl, K. A. (2008). Neural correlates of the processing of another's mistakes: a possible underpinning for social and observational learning. *Neuroimage*, 42(1):450–459.

Smith, S. M. (2002). Fast robust automated brain extraction. *Human brain mapping*, 17(3):143–155.

Smith, S. M., Jenkinson, M., Woolrich, M. W., Beckmann, C. F., Behrens, T. E., Johansen-Berg, H., Bannister, P. R., De Luca, M., Drobnjak, I., Flitney, D. E., et al. (2004). Advances in functional and structural mr image analysis and implementation as fsl. *Neuroimage*, 23:S208–S219.

Spiers, H. J. and Maguire, E. A. (2007). Decoding human brain activity during real-world experiences. *Trends in cognitive sciences*, 11(8):356–365.

Talairach, J. and Tournoux, P. (1988). *Co-Planar Stereotaxic Atlas of the Human Brain: 3-D Proportional System: An Approach to Cerebral Imaging (Thieme Classics)*. Thieme.

Taylor, S. F., Martis, B., Fitzgerald, K. D., Welsh, R. C., Abelson, J. L., Liberzon, I., Himle, J. A., and Gehring, W. J. (2006). Medial frontal cortex activity and loss-related responses to errors. *The Journal of neuroscience*, 26(15):4063–4070.

Ullsperger, M. and von Cramon, D. Y. (2001). Subprocesses of performance monitoring: a dissociation of error processing and response competition revealed by event-related fmri and erps. *Neuroimage*, 14(6):1387–1401.

Ullsperger, M. and Von Cramon, D. Y. (2004). Neuroimaging of performance monitoring: error detection and beyond. *Cortex*, 40(4):593–604.

Ullsperger, M. and von Cramon, D. Y. (2006). The role of intact frontostriatal circuits in error processing. *Journal of Cognitive Neuroscience*, 18(4):651–664.

Ursu, S., Stenger, V. A., Shear, M. K., Jones, M. R., and Carter, C. S. (2003). Overactive action monitoring in obsessive-compulsive disorder evidence from functional magnetic resonance imaging. *Psychological Science*, 14(4):347–353.

Van Essen, D. C. (2005). A population-average, landmark-and surface-based (pals) atlas of human cerebral cortex. *Neuroimage*, 28(3):635–662.

van Schie, H. T., Mars, R. B., Coles, M. G., and Bekkering, H. (2004). Modulation of activity in medial frontal and motor cortices during error observation. *Nature neuroscience*, 7(5):549–554.

van Veen, V. and Carter, C. S. (2002). The anterior cingulate as a conflict monitor: fMRI and ERP studies. *Physiology & behavior*, 77(4-5):477–82.

van Veen, V. and Carter, C. S. (2005). Separating semantic conflict and response conflict in the stroop task: a functional mri study. *Neuroimage*, 27(3):497–504.

Willemssen, R., Müller, T., Schwarz, M., Hohnsbein, J., and Falkenstein, M. (2008). Error processing in patients with parkinson's disease: the influence of medication state. *Journal of neural transmission*, 115(3):461–468.

Woolrich, M. W., Ripley, B. D., Brady, M., and Smith, S. M. (2001). Temporal autocorrelation in univariate linear modeling of fmri data. *Neuroimage*, 14(6):1370–1386.

Worsley, K. J., Taylor, J. E., Tomaiuolo, F., and Lerch, J. (2004). Unified univariate and multivariate random field theory. *Neuroimage*, 23:S189–S195.

Yu, R. and Zhou, X. (2006). Brain responses to outcomes of one's own and other's performance in a gambling task. *Neuroreport*, 17(16):1747–1751.

Appendix A: Tables of activation clusters

This appendix contains the tables representing clusters of activation in each GLM contrast image. The tables include names of the anatomical regions, numbers of corresponding Brodmann areas (BA), x-, y- and z-coordinates, hemisphere (left/right), numbers of voxels in a cluster and Z-values representing the significance of activation.

Cluster centroids are written in bold, and the other regions represent the local maxima within clusters. All coordinates are in MNI space.

Self-committed, error > baseline							
Region	**BA**	**x**	**y**	**z**	**Hemisphere**	**Voxels**	**Z-value**
ACC/Medial Frontal Cortex		**32**	**24**	**-2**	**R,L**	**8491**	
Claustrum	-	32	24	-2	R		5.97
Cingulate Gyrus	32	-2	22	30	L		5.89
Cingulate Gyrus	32	-8	20	34	L		5.53
Medial Frontal Gyrus	32	4	10	46	R		5.49
Precentral Gyrus	6	40	6	26	R		5.44
Sub-Gyral	6	20	0	58	R		5.36
Inferior Parietal Lobule/Precuneus		**36**	**-38**	**44**	**R**	**3945**	
Inferior Parietal Lobule	40	36	-38	44	R		5.28
Precuneus	7	20	-66	36	R		5.25
Precuneus	7	20	-70	48	R		5.09
Superior Temporal Gyrus	13	62	-42	16	R		4.96
Inferior Temporal Gyrus	-	46	-66	2	R		4.93
Insula	13	56	-34	18	R		4.9
Inferior Temporal Gyrus		**-46**	**-74**	**0**	**L**	**3828**	
Inferior Temporal Gyrus	37	-46	-74	0	L		5.6
Inferior Occipital Gyrus	19	-42	-82	0	L		5.1
Inferior Parietal Lobule	40	-48	-28	34	L		5.01
Inferior Occipital Gyrus	19	-40	-76	4	L		4.96
Cuneus	7	-14	-74	36	L		4.91
Middle Occipital Gyrus	19	-40	-82	8	L		4.89
Putamen		**-30**	**4**	**-2**	**L**	**2110**	
Putamen	-	-30	4	-2	L		5.22
Putamen	-	-20	4	-4	L		5.1
Precentral Gyrus	6	-54	4	12	L		4.9
Lateral Globus Pallidus	-	-12	4	4	L		4.87
Lateral Globus Pallidus	-	-10	6	-4	L		4.76
Insula	13	-44	10	-4	L		4.61
Red Nucleus		**-4**	**-28**	**-10**	**R,L**	**1180**	
Red Nucleus	-	-4	-28	-10	L		5.1
Red Nucleus	-	6	-26	-12	R		4.86
Thalamus	-	-10	-24	-2	L		4.62
Red Nucleus	-	-2	-24	-8	L		4.62
Red Nucleus	-	-8	-24	-6	L		4.56
Substantia Nigra	-	-12	-24	-10	L		4.56
Cuneus/Fusiform Gyrus		**-16**	**-78**	**-10**	**L**	**842**	
Declive	-	-16	-78	-10	L		4.79
Cuneus	18	-2	-78	10	L		4.64
Fusiform Gyrus	19	-20	-66	-8	L		4.55
Fusiform Gyrus	19	-24	-64	-6	L		4.33
Cuneus	18	-16	-70	18	L		4.17
Lingual Gyrus	18	-6	-78	4	L		4.13

Self-committed, error > correct							
Region	**BA**	**x**	**y**	**z**	**Hemisphere**	**Voxels**	**Z-value**
ACC/Medial Frontal Gyrus		**6**	**14**	**56**	**R,L**	**3530**	
Superior Frontal Gyrus	6	6	14	56	R		4.57
Medial Frontal Gyrus	6	14	10	64	R		4.26
Cingulate Gyrus	32	-4	22	30	L		4.16
Medial Frontal Gyrus	32	4	14	46	R		4.07
Precentral Gyrus	6	8	2	58	R		4.0
Middle Frontal Gyrus	6	-24	0	46	L		3.93
Insula		**32**	**26**	**0**	**R**	**2853**	
Insula	13	32	26	0	R		4.73
Extra-Nuclear	47	40	22	-8	R		4.71
Putamen	-	20	14	-6	R		4.52
Claustrum	-	32	24	-6	R		4.49
Insula	13	36	18	-10	R		4.44
Insula	13	42	20	4	R		4.21
Insula		**-44**	**10**	**-4**	**L**	**2375**	
Insula	13	-44	10	-4	L		4.12
Inferior Frontal Gyrus	47	-28	18	-18	L		4.08
Putamen	-	-30	4	-2	L		4.01
Precentral Gyrus	6	-54	6	10	L		3.93
Inferior Frontal Gyrus	47	-36	32	-6	L		3.91
Putamen	-	-20	6	-4	L		3.81
Superior Temporal Gyrus		**60**	**-40**	**18**	**L**	**646**	
Superior Temporal Gyrus	13	60	-40	18	R		3.83
Superior Temporal Gyrus	13	60	-40	22	R		3.78
Insula	13	56	-36	20	R		3.69
Superior Temporal Gyrus	13	56	-40	22	R		3.63
Inferior Parietal Lobule	40	64	-18	22	R		3.42
Superior Temporal Gyrus	39	52	-50	12	R		3.32
Postcentral Gyrus		**-66**	**-28**	**20**	**L**	**394**	
Postcentral Gyrus	40	-66	-28	20	L		4.12
Inferior Parietal Lobule	40	-60	-28	28	L		3.36
Insula	13	-50	-38	20	L		3.17
Postcentral Gyrus	2	-60	-26	42	L		3.16
Postcentral Gyrus	40	-56	-26	20	L		3.16
Superior Temporal Gyrus	22	-64	-38	20	L		3.08

Self-committed, correct > error							
Region	**BA**	**x**	**y**	**z**	**Hemisphere**	**Voxels**	**Z-value**
Caudate		**24**	**-26**	**26**	**R**	**793**	
Caudate	-	24	-26	26	R		3.47
Caudate	-	20	-18	26	R		3.43
Caudate	-	20	2	28	R		3.22
Claustrum	-	30	-12	16	R		3.2
Caudate	-	20	-6	26	R		3.17
Caudate	-	16	-14	20	R		3.14
Caudate	-	**24**	**-4**	**28**	**L**	**567**	
Claustrum	-	-28	-2	20	L		3.36
Caudate	-	-22	-28	24	L		3.36
Caudate	-	-22	-28	28	L		3.31
Medial Frontal Gyrus		**-2**	**24**	**-26**	**R,L**	**527**	
Medial Frontal Gyrus	25	-2	24	-26	L		3.88
Medial Frontal Gyrus	10	-2	46	-16	L		3.85
Medial Frontal Gyrus	11	-4	34	-20	L		3.81
Medial Frontal Gyrus	11	4	32	-22	R		3.79
Medial Frontal Gyrus	11	0	40	-24	L		3.45
Subcallosal Gyrus	25	8	24	-22	R		3.07
Putamen		**26**	**6**	**-4**	**R**	**510**	
Putamen	-	26	6	-4	R		4.35
Putamen	-	28	2	0	R		3.98
Putamen	-	24	6	2	R		3.82
Putamen	-	30	2	-4	R		3.82
Putamen	-	24	4	-12	R		3.77
Putamen	-	22	8	-12	R		3.67
Putamen	-	**28**	**6**	**-8**	**L**	**426**	
Putamen	-	-28	6	-8	L		3.94
Putamen	-	-20	8	-8	L		3.87
Putamen	-	-26	10	-4	L		3.8
Putamen	-	-28	0	-4	L		3.78
Putamen	-	-22	4	4	L		3.73
Parahippocampal Gyrus	34	-26	2	-14	L		3.67
Superior Frontal Gyrus		**-30**	**30**	**44**	**L**	**374**	
Middle Frontal Gyrus	8	-30	30	44	L		3.54
Superior Frontal Gyrus	6	-20	32	54	L		3.48
Superior Frontal Gyrus	6	-14	36	54	L		3.33
Superior Frontal Gyrus	8	-18	42	46	L		3.19
Superior Frontal Gyrus	8	-24	32	48	L		3.18
Superior Frontal Gyrus	8	-20	30	46	L		3.09

Observed game, error > baseline							
Region	**BA**	**x**	**y**	**z**	**Hemisphere**	**Voxels**	**Z-value**
Middle Temporal Gyrus		**48**	**-54**	**8**	**R**	**1206**	
Middle Temporal Gyrus	39	48	-54	8	R		4.11
Middle Temporal Gyrus	39	54	-60	8	R		4.02
Inferior Temporal Gyrus	37	54	-66	0	R		3.85
Middle Temporal Gyrus	37	50	-62	4	R		3.67
Fusiform Gyrus	37	48	-58	-18	R		3.62
Middle Temporal Gyrus	21	54	-42	12	R		3.62
Inferior Frontal Gyrus		**52**	**16**	**14**	**R**	**1006**	
Inferior Frontal Gyrus	44	52	16	14	R		4.25
Insula	13	46	16	8	R		4.17
Precentral Gyrus	44	54	14	8	R		3.85
Inferior Frontal Gyrus	44	54	20	8	R		3.75
Precentral Gyrus	44	50	10	8	R		3.7
Inferior Frontal Gyrus	47	50	18	-10	R		3.65
Fusiform Gyrus		**-38**	**-56**	**-14**	**L**	**899**	
Fusiform Gyrus	37	-38	-56	-14	L		4.08
Fusiform Gyrus	37	-44	-62	-16	L		4.07
Inferior Temporal Gyrus	37	-52	-68	2	L		3.61
Declive	-	-44	-64	-20	L		3.55
Middle Occipital Gyrus	37	-46	-70	-6	L		3.51
Inferior Temporal Gyrus	37	-46	-68	-2	L		3.5
Precuneus		**18**	**-68**	**44**	**R**	**380**	
Precuneus	7	18	-68	44	R		3.56
Superior Parietal Lobule	7	26	-62	54	R		3.56
Precuneus	7	28	-46	48	R		3.54
Precuneus	7	28	-64	32	R		3.41
Superior Parietal Lobule	7	22	-66	60	R		3.38
Inferior Parietal Lobule	40	36	-50	42	R		3.37
Superior Parietal Lobule		**-32**	**-58**	**60**	**L**	**227**	
Superior Parietal Lobule	7	-32	-58	60	L		3.51
Inferior Parietal Lobule	40	-32	-44	42	L		3.43
Superior Parietal Lobule	7	-14	-60	68	L		3.23
Inferior Parietal Lobule	40	-36	-44	50	L		3.2
Superior Parietal Lobule	7	-38	-54	60	L		3.09
Superior Parietal Lobule	7	-24	-56	66	L		3.02
Inferior Parietal Lobule		**-48**	**-40**	**54**	**L**	**222**	
Inferior Parietal Lobule	40	-48	-40	54	L		3.89
Inferior Parietal Lobule	40	-50	-36	52	L		3.86
Inferior Parietal Lobule	40	-56	-38	46	L		3.44
Inferior Parietal Lobule	40	-44	-36	38	L		2.59

Observed game, error > correct							
Region	**BA**	**x**	**y**	**z**	**Hemisphere**	**Voxels**	**Z-value**
Inferior Frontal Gyrus		**46**	**14**	**8**	**R**	**384**	
Insula	13	46	14	8	R		3.46
Inferior Frontal Gyrus	45	50	16	14	R		3.33
Inferior Frontal Gyrus	9	44	14	20	R		3.23
Precentral Gyrus	44	52	10	8	R		3.22
Inferior Frontal Gyrus	44	54	20	6	R		3.18
Middle Frontal Gyrus	9	50	18	26	R		3.03

Naturalistic, error > baseline							
Region	**BA**	**x**	**y**	**z**	**Hemisphere**	**Voxels**	**Z-value**
Visual cortex/Cerebellum		**-12**	**-74**	**-12**	**R,L**	**12308**	
Declive	-	-12	-74	-12	L		4.87
Declive	-	-18	-76	-16	L		4.79
Culmen	-	8	-72	-6	R		4.67
Lingual Gyrus	18	-12	-80	2	L		4.66
Lingual Gyrus	18	-2	-84	2	L		4.64
Culmen	-	-8	-72	-6	L		4.53
Middle Temporal Gyrus		**52**	**8**	**-32**	**R**	**3092**	
Middle Temporal Gyrus	21	52	8	-32	R		4.41
Superior Temporal Gyrus	38	52	6	-28	R		4.34
Sub-Gyral	21	46	-12	-16	R		4.21
Superior Temporal Gyrus	21	58	-6	-16	R		3.96
Middle Temporal Gyrus	21	52	-2	-26	R		3.92
Inferior Frontal Gyrus	47	44	24	-22	R		3.91
Medial Frontal Gyrus		**0**	**48**	**24**	**R,L**	**1456**	
Medial Frontal Gyrus	9	0	48	24	L		3.6
Medial Frontal Gyrus	9	-8	50	24	L		3.41
Medial Frontal Gyrus	9	-6	50	12	L		3.39
Medial Frontal Gyrus	9	4	58	12	R		3.38
Medial Frontal Gyrus	9	-2	48	12	L		3.31
Medial Frontal Gyrus	10	6	62	16	R		3.3
Middle Temporal Gyrus		**-54**	**2**	**-20**	**L**	**378**	
Middle Temporal Gyrus	21	-54	2	-20	L		3.65
Middle Temporal Gyrus	21	-56	6	-30	L		3.45
Middle Temporal Gyrus	21	-54	8	-24	L		3.32
Middle Temporal Gyrus	21	-50	-20	-18	L		3.26
Middle Temporal Gyrus	21	-58	-8	-20	L		3.25
Middle Temporal Gyrus	21	-60	-20	-16	L		3.19

Naturalistic, error > pain							
Region	**BA**	**x**	**y**	**z**	**Hemisphere**	**Voxels**	**Z-value**
Visual cortex/cerebellum		**-26**	**-70**	**-16**	**R,L**	**21012**	
Lingual Gyrus	18	12	-72	6	R		4.89
Declive	-	-26	-70	-16	L		4.89
Declive	-	-28	-64	-14	L		4.73
Lingual Gyrus	18	10	-76	0	L		4.71
Lingual Gyrus	-	-4	-84	4	L		4.66
Culmen	-	10	-74	-6	R		4.63
ACC/Medial Frontal Gyrus		**0**	**30**	**34**	**L**	**1497**	
Cingulate Gyrus	32	0	30	34	L		3.43
Medial Frontal Gyrus	9	0	48	24	L		3.37
Medial Frontal Gyrus	8	-8	28	46	L		3.34
Cingulate Gyrus	32	0	40	24	L		3.27
Superior Frontal Gyrus	9	-2	62	28	L		3.26
Cingulate Gyrus	24	-6	22	24	L		3.25
Middle Temporal Gyrus		**38**	**-62**	**32**	**R**	**653**	
Middle Temporal Gyrus	39	38	-62	32	R		3.42
Angular Gyrus	39	44	-62	40	R		3.36
Precuneus	39	40	-64	38	R		3.35
Angular Gyrus	39	46	-56	24	R		3.35
Middle Temporal Gyrus	39	44	-60	24	R		3.32
Middle Occipital Gyrus	19	36	-82	16	R		3.31
Middle Frontal Gyrus		**-26**	**18**	**36**	**L**	**591**	
Middle Frontal Gyrus	8	-26	18	36	L		3.86
Precentral Gyrus	9	-40	10	38	L		3.51
Sub-Gyral	8	-18	26	38	L		3.5
Middle Frontal Gyrus	9	-42	14	40	L		3.49
Middle Frontal Gyrus	8	-28	24	46	L		3.38
Precentral Gyrus	9	-36	28	38	L		3.14
Middle Temporal Gyrus		**-50**	**-16**	**-20**	**L**	**582**	
Sub-Gyral	20	-50	-16	-20	L		3.62
Middle Temporal Gyrus	21	-58	-6	-20	L		3.55
Fusiform Gyrus	20	-64	-20	-30	L		3.45
Middle Temporal Gyrus	21	-58	-12	-14	L		3.41
Inferior Temporal Gyrus	20	-64	-26	-20	L		3.35
Middle Temporal Gyrus	21	-62	-26	-12	L		3.23

Self-committed > Observed game							
Region	**BA**	**x**	**y**	**z**	**Hemisphere**	**Voxels**	**Z-value**
ACC/Medial Frontal Cortex		**6**	**2**	**46**	**R,L**	**20933**	
Cingulate Gyrus	24	6	2	46	R		4.76
Precentral Gyrus	6	36	-8	54	R		4.7
Medial Frontal Gyrus	6	-6	4	52	L		4.65
Medial Frontal Gyrus	6	8	4	54	R		4.64
Precentral Gyrus	4	-38	-12	50	L		4.63
Cingulate Gyrus	24	4	8	34	R		4.6
Putamen		**18**	**12**	**-6**	**R,L**	**5608**	
Putamen	-	18	12	-6	R		4.98
Putamen	-	-20	8	-6	L		4.75
Putamen	-	-30	6	-4	L		4.7
Red Nucleus	-	6	-18	-18	R		4.23
Globus Pallidus	-	-12	4	4	L		4.12
Precentral Gyrus		**-54**	**0**	**20**	**L**	**267**	
Precentral Gyrus	6	-54	0	20	L		3.49
Precentral Gyrus	6	-58	6	28	L		3.37
Precentral Gyrus	6	-54	4	8	L		3.1
Precentral Gyrus	6	-54	4	12	L		3.09
Precentral Gyrus	6	-60	4	6	L		3.01
Precentral Gyrus	6	-52	4	26	L		2.92

Naturalistic > Observed game							
Region	**BA**	**x**	**y**	**z**	**Hemisphere**	**Voxels**	**Z-value**
Precuneus/Lingual Gyrus		**0**	**-62**	**22**	**L**	**5554**	
Precuneus	23	0	-62	22	L		5
Posterior Cingulate	30	0	-64	16	L		4.64
Lingual Gyrus	18	-2	-80	2	L		4.62
Lingual Gyrus	-	-6	-82	4	L		4.55
Culmen	-	-10	-72	-6	L		4.55
Lingual Gyrus	18	-4	-76	2	L		4.54
ACC/Medial Frontal Gyrus		**-2**	**24**	**-22**	**R,L**	**1080**	
Medial Frontal Gyrus	25	-2	24	-22	L		3.85
Superior Frontal Gyrus	9	0	60	26	L		3.65
Anterior Cingulate	24	-8	30	-6	L		3.48
Caudate	-	-6	26	-4	L		3.39
Medial Frontal Gyrus	10	-8	42	-16	L		3.18
Anterior Cingulate	32	6	42	-16	R		3.16
Parahippocampal Gyrus		**-22**	**-38**	**-14**	**L**	**564**	
Culmen	-	-22	-38	-14	L		3.69
Amygdala	-	-30	-6	-24	L		3.62
Substantia Nigra	-	-14	-18	-14	L		3.4
Parahippocampal Gyrus	35	-24	-26	-22	L		3.36
Parahippocampal Gyrus	28	-24	-22	-16	L		3.34
Parahippocampal Gyrus	36	-32	-36	-18	L		3.33
Middle Temporal Gyrus		**-48**	**-12**	**-18**	**L**	**349**	
Sub-Gyral	21	-48	-12	-18	L		3.74
Superior Temporal Gyrus	22	-50	-12	-14	L		3.35
Middle Temporal Gyrus	21	-54	-14	-24	L		3.25
Sub-Gyral	20	-50	-20	-20	L		3.19
Middle Temporal Gyrus	21	-54	2	-20	L		3.14
Middle Temporal Gyrus	21	-54	-4	-14	L		3.05
Observed game > Naturalistic							
Superior Parietal Lobule		**-24**	**-56**	**66**	**L**	**477**	
Superior Parietal Lobule	7	-24	-56	66	L		4.36
Inferior Parietal Lobule	40	-40	-46	62	L		3.86
Inferior Parietal Lobule	40	-48	-42	56	L		3.73
Superior Parietal Lobule	7	-30	-52	64	L		3.64
Superior Parietal Lobule	7	-14	-60	68	L		3.51
Inferior Parietal Lobule	40	-52	-34	50	L		3.42
Inferior Frontal Gyrus		**56**	**12**	**8**	**R**	**248**	
Precentral Gyrus	44	56	12	8	R		3.77
Insula	13	46	16	8	R		3.67
Inferior Frontal Gyrus	44	54	18	10	R		3.2
Inferior Frontal Gyrus	9	48	8	18	R		3.18
Inferior Frontal Gyrus	44	54	20	6	R		3.09
Inferior Frontal Gyrus	44	58	20	16	R		2.94

Self-committed > Naturalistic							
Region	**BA**	**x**	**y**	**z**	**Hemisphere**	**Voxels**	**Z-value**
Medial Frontal Cortex		**-4**	**4**	**52**	**R,L**	**28808**	
Medial Frontal Gyrus	6	-4	4	52	L		5.95
Claustrum	-	32	24	-2	R		5.71
Medial Frontal Gyrus	6	-4	0	56	L		5.67
Sub-Gyral	6	20	0	58	R		5.51
Middle Frontal Gyrus	6	-30	-2	50	L		5.48
Medial Frontal Gyrus	6	8	-4	62	R		5.41
Red Nucleus		**-8**	**-22**	**-6**	**R,L**	**997**	
Red Nucleus	-	-8	-22	-6	L		4.15
Substantia Nigra	-	-6	-16	-12	L		4.11
Red Nucleus	-	-4	-26	-12	L		4.09
Red Nucleus	-	8	-26	-14	R		3.88
Thalamus	-	10	-14	-2	R		3.61
Red Nucleus	-	6	-16	-14	R		3.56
Inferior Temporal Gyrus		**46**	**-64**	**2**	**R**	**577**	
Inferior Temporal Gyrus	-	46	-64	2	R		3.94
Inferior Temporal Gyrus	37	48	-52	-2	R		3.9
Middle Temporal Gyrus	39	46	-56	6	R		3.79
Sub-Gyral	-	42	-56	0	R		3.63
Sub-Gyral	-	38	-66	4	R		3.5
Inferior Temporal Gyrus	19	52	-58	0	R		3.4
Middle Frontal Gyrus		**36**	**44**	**18**	**R**	**575**	
Middle Frontal Gyrus	10	36	44	18	R		4.04
Middle Frontal Gyrus	10	40	42	8	R		3.66
Middle Frontal Gyrus	10	38	48	8	R		3.55
Middle Frontal Gyrus	9	36	36	24	R		3.5
Middle Frontal Gyrus	9	40	30	24	R		3.4
Superior Frontal Gyrus	10	42	56	12	R		3.3

Naturalistic > Self-committed							
Region	**BA**	**x**	**y**	**z**	**Hemisphere**	**Voxels**	**Z-value**
Posterior Cingulate		**-4**	**-42**	**32**	**R,L**	**857**	
Cingulate Gyrus	31	-4	-42	32	L		4.22
Cingulate Gyrus	31	-10	-50	24	L		4.12
Posterior Cingulate	31	-8	-50	20	L		4.06
Posterior Cingulate	23	4	-52	18	R		3.95
Cingulate Gyrus	31	2	-34	32	R		3.61
Precuneus	31	4	-46	32	R		3.47
Superior Frontal Gyrus		**0**	**48**	**26**	**R,L**	**543**	
Medial Frontal Gyrus	9	0	48	26	L		3.94
Superior Frontal Gyrus	9	-12	56	32	L		3.77
Superior Frontal Gyrus	8	-8	48	40	L		3.63
Superior Frontal Gyrus	9	-8	52	34	L		3.6
Superior Frontal Gyrus	9	12	58	26	R		3.22
Medial Frontal Gyrus	10	4	62	14	R		3.15
Superior Temporal Gyrus		**46**	**-64**	**40**	**R**	**221**	
Inferior Parietal Lobule	39	46	-64	40	R		3.54
Angular Gyrus	39	52	-60	34	R		3.27
Superior Temporal Gyrus	39	52	-58	30	R		3.21
Supramarginal Gyrus	40	60	-54	26	R		3.08
Superior Temporal Gyrus	39	52	-56	24	R		3.05
Supramarginal Gyrus	40	54	-54	30	R		3.04

Anticipation > baseline							
Region	**BA**	**x**	**y**	**z**	**Hemisphere**	**Voxels**	**Z-value**
ACC/Medial Frontal Gyrus		**-6**	**-10**	**64**	**L**	**1759**	
Medial Frontal Gyrus	6	-6	-10	64	L		3.69
Paracentral Lobule	31	-6	-18	44	L		3.66
Medial Frontal Gyrus	6	0	-4	52	L		3.56
Medial Frontal Gyrus	6	-4	-6	56	L		3.5
Medial Frontal Gyrus	6	-8	-8	60	L		3.42
Cingulate Gyrus	24	-8	0	38	L		3.42
Insula/Inferior Frontal Gyrus		**-46**	**8**	**4**	**L**	**1548**	
Precentral Gyrus	44	-46	8	4	L		3.81
Inferior Frontal Gyrus	47	-44	22	-2	L		3.7
Inferior Frontal Gyrus	47	-42	22	-6	L		3.66
Insula	13	-42	4	-4	L		3.63
Insula	13	-46	0	0	L		3.6
Precentral Gyrus	44	-42	8	2	L		3.5
Precentral Gyrus		**52**	**8**	**6**	**L**	**1451**	
Precentral Gyrus	44	52	8	6	R		3.9
Superior Temporal Gyrus	22	54	10	2	R		3.77
Inferior Frontal Gyrus	47	38	30	-10	R		3.61
Claustrum	-	38	4	-4	R		3.6
Insula	-	38	20	-2	R		3.59
Inferior Frontal Gyrus	47	34	22	-10	R		3.57
Inferior Parietal Lobule		**42**	**-34**	**50**	**R**	**508**	
Inferior Parietal Lobule	40	42	-34	50	R		3.54
Precuneus	7	14	-62	54	R		3.34
Postcentral Gyrus	5	38	-42	64	R		3.34
Superior Parietal Lobule	7	22	-48	64	R		3.31
Superior Parietal Lobule	7	28	-48	62	R		3.29
Precuneus	7	20	-56	54	R		3.28
Insula/Postcentral gyrus		**54**	**-18**	**26**	**R**	**416**	
Insula	13	54	-18	26	R		3.64
Postcentral Gyrus	2	62	-18	34	R		3.41
Postcentral Gyrus	40	64	-26	20	R		3.39
Postcentral Gyrus	2	58	-20	34	R		3.36
Inferior Parietal Lobule	40	60	-28	30	R		3.33
Insula	13	54	-30	22	R		3.3
Insula/Postcentral gyrus		**-58**	**-20**	**18**	**L**	**365**	
Postcentral Gyrus	40	-58	-20	18	L		3.52
Insula	13	-52	-30	20	L		3.49
Postcentral Gyrus	2	-56	-22	38	L		3.36
Postcentral Gyrus	2	-60	-20	32	L		3.14
Inferior Parietal Lobule	40	-58	-24	30	L		3.13
Postcentral Gyrus	3	-60	-20	44	L		3.11
Fusiform Gyrus		**50**	**-64**	**-8**	**R**	**205**	
Fusiform Gyrus	37	50	-64	-8	R		3.57
Inferior Temporal Gyrus	37	52	-54	-4	R		3.33
Middle Temporal Gyrus	37	56	-60	-10	R		2.98
Middle Occipital Gyrus	19	56	-60	-4	R		2.9
Fusiform Gyrus	19	44	-70	-6	R		2.85

Anticipation > Error							
Region	**BA**	**x**	**y**	**z**	**Hemisphere**	**Voxels**	**Z-value**
Middle Frontal Gyrus		**-24**	**-4**	**56**	**L**	**1839**	
Middle Frontal Gyrus	6	-24	-4	56	L		3.98
Sub-Gyral	6	-18	-2	54	L		3.88
Middle Frontal Gyrus	6	-22	-12	62	L		3.87
Precentral Gyrus	6	-24	-12	66	L		3.69
Middle Frontal Gyrus	6	-20	-2	50	L		3.62
Medial Frontal Gyrus	6	-10	-4	60	L		3.59
Postcentral Gyrus/Precuneus		**-24**	**-48**	**60**	**L**	**892**	
Sub-Gyral	7	-24	-48	60	L		3.66
Postcentral Gyrus	5	-30	-42	64	L		3.62
Inferior Parietal Lobule	40	-40	-38	60	L		3.52
Precuneus	7	-8	-56	66	L		3.52
Inferior Parietal Lobule	40	-30	-36	54	L		3.43
Precuneus	7	-16	-50	62	L		3.39
Insula		**-46**	**0**	**2**	**L**	**800**	
Insula	13	-46	0	2	L		3.69
Superior Temporal Gyrus	22	-52	0	0	L		3.59
Inferior Frontal Gyrus	47	-32	22	-14	L		3.4
Insula	-	-42	22	-4	L		3.38
Insula	13	-38	-4	12	L		3.33
Extra-Nuclear	47	-34	22	-6	L		3.23
Brainstem		**-6**	**-30**	**-10**	**R,L**	**629**	
Brainstem	-	-6	-30	-10	L		3.43
Brainstem	-	8	-30	-14	R		3.37
Postcentral Gyrus		**40**	**-38**	**64**	**R**	**553**	
Postcentral Gyrus	5	40	-38	64	R		3.35
Postcentral Gyrus	5	40	-44	62	R		3.33
Inferior Parietal Lobule	40	36	-36	54	R		3.31
Postcentral Gyrus	3	34	-34	50	R		3.3
Superior Parietal Lobule	7	34	-50	62	R		3.29
Inferior Parietal Lobule	40	36	-38	58	R		3.27

Error > Anticipation							
Region	**BA**	**x**	**y**	**z**	**Hemisphere**	**Voxels**	**Z-value**
Visual cortex/Cerebellum		**-10**	**-80**	**2**	**L**	**4823**	
Lingual Gyrus	-	-10	-80	2	L		4.33
Declive	-	-10	-76	-12	L		4.03
Cuneus	17	12	-94	6	R		3.98
Declive	-	-18	-78	-16	L		3.93
Declive	-	-30	-72	-14	L		3.87
Culmen	-	-10	-72	-6	L		3.85
ACC		**-8**	**48**	**2**	**R,L**	**518**	
Anterior Cingulate	32	-8	48	2	L		3.46
Anterior Cingulate	24	4	38	-8	R		3.34
Medial Frontal Gyrus	10	-10	46	8	L		3.33
Anterior Cingulate	32	-4	42	8	L		3.08
Anterior Cingulate	24	-6	42	2	L		3.08
Anterior Cingulate	32	8	38	-12	R		3.06
Putamen		**26**	**10**	**-14**	**R**	**355**	
Putamen	-	26	10	-14	R		3.51
Putamen	-	28	8	-10	R		3.44
Claustrum	-	32	8	-14	R		3.34
Claustrum	-	36	0	-14	R		3.33
Amygdala	-	38	-6	-16	R		3.32
Putamen	-	32	6	-10	R		3.25

Surprising > Anticipated							
Region	**BA**	**x**	**y**	**z**	**Hemisphere**	**Voxels**	**Z-value**
ACC/Medial Frontal Gyrus		**-2**	**54**	**28**	**R,L**	**254**	
Superior Frontal Gyrus	9	-2	54	28	L		3.56
Anterior Cingulate	32	-2	46	12	L		3.34
Medial Frontal Gyrus	9	-2	56	20	L		3.18
Medial Frontal Gyrus	9	4	44	28	R		2.85
Medial Frontal Gyrus	9	-6	46	28	L		2.8
Medial Frontal Gyrus	8	-8	40	36	L		2.78
Anticipated > Surprising							
Cuneus/Lingual Gyrus		**10**	**-86**	**8**	**R**	**7460**	
Cuneus	17	10	-86	8	R		5.14
Lingual Gyrus	18	12	-80	6	R		4.88
Cuneus	18	8	-90	14	R		4.53
Culmen	-	14	-72	-8	R		4.36
Lingual Gyrus	18	10	-72	2	R		4.35
Lingual Gyrus	18	10	-78	-6	R		4.28
Precuneus		**32**	**-60**	**34**	**R**	**289**	
Precuneus	7	32	-60	34	R		4
Superior Parietal Lobule	7	26	-60	50	R		3.94
Sub-Gyral	39	34	-58	44	R		3.46
Superior Parietal Lobule	7	34	-58	56	R		3.06
Precuneus	7	24	-58	40	R		2.85
Precuneus	7	26	-62	42	R		2.67